Effect of a uniform through-surface flow on the force acting on a rigid body

By C.A. KLETTNER†, I. EAMES, S. SEMSARZADEH
AND A. NICOLLE

[1]University College London, Torrington Place, London, WC1E 6BT, U.K.

The effect of a uniform through-surface flow of velocity U_b on a rigid cylinder and sphere (of radius a) fixed in a stream with speed U_∞ is analysed analytically and numerically. The flow is characterised by a dimensionless blow velocity $\Lambda = U_b/U_\infty$ and Reynolds number $Re = 2aU_\infty/\nu$, where ν is the kinematic viscosity.

For a $-\Lambda \ll 1$, the flow is viscously dominated in a thin boundary layer of thickness $\nu/|U_b|$ adjacent to the rigid surface which develops in a time ν/U_b^2; the surface vorticity scales as $U_b\nu/U_\infty a^2$. A boundary layer analysis is developed to analyse the unsteady viscous forces. For the steady state, numerical calculations of the pressure on the surface of the body corresponds to the irrotational solution and the distribution of vorticity within the boundary layer and on the surface of the bodies agrees with a steady state analysis. The flow downstream of the body is irrotational so the wake volume flux, Q_w, is zero and the drag force is $F_D = -\rho U_\infty Q_b$, where Q_b is the normal flux through the body surface. This shows that the drag coefficient is $-2\pi\Lambda$ or -8Λ for a cylinder or sphere, respectively. A dissipation argument is applied to analyse the force; the rate of working of the drag force is balanced by dissipation and flux of energy and rate of work by viscous stresses due to sucking. For a cylinder, the force is determined by dissipation, with a weak contribution by the normal viscous stresses, while for a sphere, only 3/4 of the force is determined by dissipation. This analysis confirms the drag coefficients.

When $-\Lambda \gg 1$, the boundary layer thickness initially grows linearly with time as vorticity is blown away from the rigid surfaces. The initial decay of the total force is due to viscous effects. For later time, the blow velocity causes the shed vorticity to separate, significantly increasing the wake volume flux. The vorticity in the vicinity of the rigid body is weakly dependent on viscosity and this is estimated using a boundary layer analysis. The surface vorticity scales as $U_\infty^2/2aU_b$ and so that the flux of vorticity has a weak dependence on the blow velocity. For large blow velocity, the vorticity is swept into two well-separated shear layers and the maximum vorticity decreases due to diffusion. From global momentum consideration, the drag force is $F_D = \rho U_\infty(Q_w - Q_b)$ and has a weak dependence on blow velocity. The total drag is weakly dependent on U_b and decreases for a sphere.

High resolution numerical calculations are compared against the theoretical predictions over the range $-3 \le \Lambda \le 3$ and $Re = 1, 10, 100$ for planar flow past a cylinder and axisymmetric flow past a sphere.

---

† Email address for correspondence: c.klettner@ucl.ac.uk

1. Introduction

A rigid surface imposes two boundary conditions on a Newtonian fluid - a normal or kinematic boundary condition (which can be derived from mass conservation) and a tangential boundary condition based on (indirect) empirical evidence (see Reynolds (1886), Batchelor (1967), Lauga, Brenner & Stone 2007). In most problems, the kinematic boundary condition reduces to the relative velocity normal to the wall being zero. There are a number of important practical cases where a through-surface flow is either deliberately introduced because it has a beneficial effect or is a consequence of other processes present. These examples include:

a) cooling turbine blades. The thermodynamic efficiency of combustion is usually increased by raising the temperature of the reaction. To cope with raised temperatures, the surface properties of turbine blades are modified by coating with a ceramic (Goward 1998) or by introducing a flow through surface holes near the leading edge of the blades (Bogard & Thole 2006). The through surface flow serves two purposes - first the air flows through the internal structure of the blades and cools the blade internally (Iacovides & Launder 1995), and second, the flow introduced at the leading edge displaces both the velocity and thermal boundary layer away from the blade surface reducing the rate of heat transfer. There is also evidence that introducing a blow flow near to the tip of the turbine blade reduces the pressure drop by altering flow near the tip gap.

b) controlling the forces on a rigid body. Applying suction to various parts of a lifting surface of an aerofoil can be used to increase lift by preventing flow separation and stall. Likewise, applying a blowing flow can serve to increase drag, for instance, by acting as an air break. In many cases the flow is directed with a tangential component parallel to the body surface (Nishino & Shariff 2012), either through a slot or holes.

c) phase changes. The evaporation of a fuel droplet leads to it shrinking in time which generates a change in the volume of the dispersed phase and an associated through-surface flux (Cowe 1976). The current trend is for direct injection internal combustion engines where the fuel is injected at pressure, over a short period, to atomise fuel (Zhao, Harrington & Lai 2002). The fuel droplets are typically sufficiently small that the characteristic Reynolds number is smaller than 50. Likewise, the condensation of vapour bubbles generated by boiling a liquid leads to a relative flow towards the bubble surface, but since this relative speed is proportional to the ratio of vapour to fluid density, its dynamical influence is negligible (Eames 2010).

In examples (a) and (b), the through-surface flow is usually applied over a portion of the surface of a body surface. The focus in this paper is on the influence of a through-surface flow applied over the whole of the surface of a bluff body, specifically focussing on a cylinder and sphere, as this serves as a natural starting point to understand the general influence of a through-surface flow applied to portions of a rigid body. Specifically we consider the flow past a rigid surface with an outward flow U_b, normal to the surface. The flow is characterized by a dimensionless blow velocity $\Lambda = U_b/U_\infty$ (to use the terminology of the combustion literature); for blowing $\Lambda > 0$, and for suction $\Lambda < 0$. As a way of identifying gaps in the previous studies, a scatter plot of the parameter range which have been analysed to date is shown in figure 1. The first observation is that the effect of strong sucking flows has not be analysed in great detail numerically or analytically, although there were some excellent experimental studies in the 1950's on cylinders. As we shall see, this is because the boundary layer is extremely thin for $\Lambda < -1$ and the size of the computational domain has a significant and anticipated effect on the force calculation, especially for two-dimensional flows. The second observation is that the unsteady and transient component of the flow and forces has not been analysed

although this is essential for understanding the progression to steady state. These two gaps form the basis of this paper.

Our discussion of the specific contributions to the research literature starts with the case of a cylinder, before proceeding to a sphere. Considerable amount of research was undertaken in the 1950's to examine the flow and wake profiles behind a porous cylinder (Pankhurst & Thwaites 1953, Hurley & Thwaites 1951). They showed that for large suction the boundary layer is thin and the flow outside the boundary layer largely irrotational, with the pressure distribution corresponding to the irrotational prediction. A number of remarkable papers emerged during this period because of the interest in controlling the boundary layer. More recent experimental analysis of the flow and forces generated by weakly blowing and sucking porous cylinders were undertaken by Fransson, Konieczny & Alfredsson (2004). Fransson *et al.* (2004) analysed the drag force by direct measurement and by evaluating the volume flux in the wake and using Betz relation to infer the drag force. In circumstances where there is a through-surface flow (and no thrust) Betz (1925) relationship is invalid (as we discuss later) explaining the difference between these two measurements. Even for the relatively low through-surface flow velocity, Fransson *et al.* (2004) demonstrated the rather significant effect of blowing on the boundary layer and the force on the body. Mathelin, Bataille & Lallemand (2002) examined the flow past a cylinder a higher Re and concluded that the drag force on a cylinder increases due to blowing, in contrast to a sphere. However, the domain size was small and its influence on the drag force needs to be assessed.

For the case of a sphere, Cliffe & Lever (1985) developed a comprehensive numerical study of a radial through-surface flow ($\Lambda > 0$) at moderate Reynolds numbers (< 100) for an axisymmetric flow past a sphere. They developed a technique that enabled them to account for an unbounded domain. The physical insight they provided is really quite excellent which they cast in terms of the surface vorticity field, largely because the solution technique employed a vorticity-streamfunction formulation. Much of the discussion in our paper is in relation to the vorticity field as it provides a clear indication on how the no-slip condition modifies the primary irrotational solution. Also noteworthy is the analytical work of Dukowicz (1982) who derived an exact solution for Stokes flow past a sphere with uniform blowing and sucking. Even for moderately large Reynolds numbers and small $|\Lambda|$ the flow is ultimately three-dimensional and the component of lift must also be considered. Baghchi (2007) studied the effects of uniform surface blowing and suction on the drag and lift forces on a sphere in the range $1 < Re < 300$ and $|\Lambda| < 0.2$. Baghchi (2007) categorised the wake flow in terms of the unsteady components of the lift and drag using a reasonably high resolution of the flow.

Figure 1 shows a scatter plot summarising the research on uniform through-surface flows for cylinder and spheres. For large $|\Lambda|$, a fully resolved three-dimensional calculation seems to be still too formidable to tackle which is why we restrict our attention to axisymmetric flows at low to moderate Reynolds numbers past a sphere, where the assumption of axisymmetry is still appropriate. Nevertheless, the allied scaling analysis and analytical models that we present provide a strong indication of what is to be expected for Reynolds numbers greater than 100 and $|\Lambda| > 1$.

The paper is structured as follows. The general problem is stated in §2, where the general feature of the forces and their relationship to the through-surface flow are identified. A mathematical analysis is developed for the boundary layer flow generated by blowing and sucking, which identifies the initial characteristics of the force. For strong sucking inertially dominated flows, the flow is characterised by a thin boundary layer and the analysis is valid for long time, while for blowing flows, the analysis is valid only when the boundary layer is thin or short time. This analysis provides a means of interpreting the
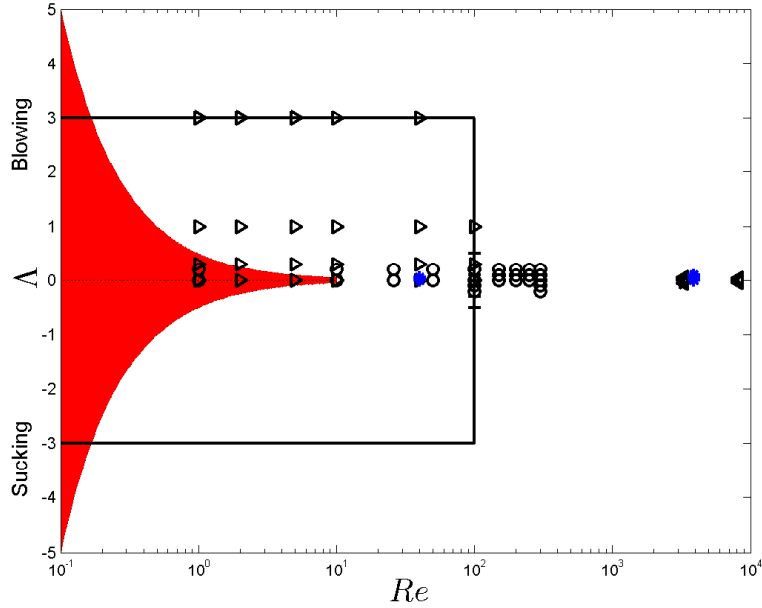
Figure 1: Scatter plot showing a summary of the research on blowing / sucking flow past a cylinder and sphere. The symbols correspond to ∘ (Baghchi (2007), sphere, numerics), + (Ling & Fang 2002, cylinder, numerics), ◁ (Fransson *et al.* (2004), cylinder, experiments), ▷ (Cliffe & Lever (1982), sphere, numerics), △ Bashkatov & Shabanov (1975) (sphere, numerics), ∗ (Mathelin *et al.* 2002, cylinder, numerics). The red field represents the validity of Dukowicz's (1981) low *Re* analytical solution. The bounding box indicates the parameter space investigated in this paper.

force and flow for times between the blowing viscous and blowing inertial times scales. A weakly viscous analysis is developed to understand the features of the vorticity field far downstream and estimate how strong blowing affects the force on a cylinder and sphere. To test the analytical results, a numerical study was performed for planar and axisymetric flow, as discussed in §3 and are compared against analytical results from §2. The results are discussed within a general context in §4 §7, before concluding in §8.

2. Mathematical model

For a rigid body moving with velocity $\boldsymbol{v}$, we are exploring the general influence of the kinematic boundary condition

$$(\boldsymbol{u} - \boldsymbol{v}) \cdot \hat{\boldsymbol{n}} = -U_b, \tag{2.1}$$

imposed on the whole of the body surface, where $\boldsymbol{u}$ is the flow velocity and $\hat{\boldsymbol{n}}$ is the unit normal vector pointing into the body surface. The no-slip condition reduces to

$$(\boldsymbol{u} - \boldsymbol{v}) \cdot \hat{\boldsymbol{s}} = 0, \tag{2.2}$$

where $\hat{\boldsymbol{s}}$ is the unit vector tangential to the body surface. Two cases are considered - rigid cylinder and sphere (both of radius a) for which we can identify a Reynolds number $Re = 2U_\infty a/\nu$.

2.1. *General considerations*

For a uniform through-surface flow, the force on a rigid body with surface S_B is defined as

$$\boldsymbol{F} = \int_{S_B} (p\boldsymbol{I} - \boldsymbol{\tau}) \cdot \hat{\boldsymbol{n}} \mathrm{d}S, \tag{2.3}$$

(Legendre, Moree & Magnaudet 1997), where p is the pressure and $\boldsymbol{\tau}$ is the viscous stress tensor. (The momentum flux from the uniform through-surface component is $-\int_{S_B} \rho\boldsymbol{u}(\boldsymbol{u}\cdot\hat{\boldsymbol{n}})\mathrm{d}S = \boldsymbol{0}$.) For the case of an incident flow $\boldsymbol{U} = U_\infty\hat{\boldsymbol{x}}$, the drag coefficients is defined as

$$C_D(t) = \frac{\boldsymbol{F} \cdot \hat{\boldsymbol{x}}}{\frac{1}{2}\rho A U_\infty^2}, \tag{2.4}$$

where $\hat{\boldsymbol{x}}$ is a unit vector in the streamwise direction and A is the projected cross-sectional area (or width) of the body and is equal to $2a$, πa^2 for a cylinder/sphere respectively.

For steady flows, the steady drag force can be expressed more generally in terms of the volume flux in the wake and source flow. Eames & Hunt (2002) showed that in general, the drag force on a body (with no momentum flux through the body surface) is

$$F_D = -\rho Q_s U_\infty + 2\rho Q_w U_\infty, \tag{2.5}$$

where ρ is density, Q_w is the volume flux in the narrow downstream wake and Q_s is the source flow generated by the body (the first term is usually described as the Lamb force - Lamb 1932). When $U_b = 0$, the source flow is equal to the volume flux in the wake $Q_w = Q_s$ and (2.5) reduces to the classic result attributed to Betz (1925):

$$F_D = \rho Q_w U_\infty. \tag{2.6}$$

For a strong uniform sucking flow $(-\Lambda \gg 1)$, the boundary thickness for both cylinder and sphere scale as $\nu/|U_b|$ and the boundary layer is thin. Because the flow is irrotational outside the thin attached boundary layer and downstream of the body, the wake volume flux Q_w will tend to zero as $\Lambda \to -\infty$, so that the drag force tends to

$$F_D = -\rho A_b U_b U_\infty (> 0), \tag{2.7}$$

where A_b is the surface area of the rigid body. The integral approach provides details of the drag force but does not give any insight into the flow field. The expression (2.7) was also derived by Pankhurst & Thwaites (1950, Appendix I) for flow with large suction and no thrust.

Much less general information can be gleamed for the case of a strong blow flow $(\Lambda \gg 1)$. From the general discussion of forces, the source flux Q_s is a combination of the wake and blowing flux, $Q_s = Q_w + Q_b$, which combined with (2.5) gives

$$F_D = \rho U_\infty (Q_w - A_b U_b), \tag{2.8}$$

(also obtained by Cliffe & Lever (1985, eqn. 17)). As we shall see, the blow flow causes the wake width to widen so that the wake volume flux increases with the blow flow, *i.e.* $Q_w \sim A_b U_b$ and that the drag force is not as strongly affected by Λ as compared to the dramatic effect of sucking the boundary layer through the body surface.

The kinematic effect of the rigid surface generates a source flow in the far field and a dipole contribution for a cylinder or sphere. The irrotational solution, $\boldsymbol{u} = \boldsymbol{\nabla}\phi$, is well-known for a cascade of complexity from a uniform flow past a rigid plate

$$\phi(r, \theta) = U_\infty r \cos\theta + U_b r \sin\theta, \tag{2.9}$$

(which we place at $y = a$) for a cylinder

$$\phi(r, \theta) = U_\infty r \cos\theta \left(1 + \frac{a^2}{r^2}\right) + U_b a \log r, \tag{2.10}$$

and a sphere,

$$\phi(r, \theta) = U_\infty r \cos\theta \left(1 + \frac{a^3}{2r^3}\right) - \frac{U_b a}{r}. \tag{2.11}$$

The slip at the surface of the rigid body in a potential flow is, $\partial\phi/\partial s|_{r=a} = -U_\infty$, $-2U_\infty \sin\theta$, $-(3/2)U_\infty \sin\theta$, (where $s = a\theta$ for a cylinder and sphere). To examine the influence of this component, we decompose the velocity into a primary irrotational component and a rotational component to enforce the no slip condition on the rigid surfaces, *i.e.*

$$\boldsymbol{u} = \boldsymbol{\nabla}\phi + \boldsymbol{u}_R(\boldsymbol{x}, t). \tag{2.12}$$

The purpose of the discussion in this section is to examine the form and role of the rotational component of the flow, using a boundary layer analysis for short time, and a viscous description for blowing for long time. Much of the discussion will center around the short blowing viscous (T_ν) and inertial (T_b) time scales set by the blow velocity and the advective time scale (T_a) defined as

$$T_\nu = \frac{\nu}{U_b^2}, \qquad T_b = \frac{a}{|U_b|}, \qquad T_a = \frac{a}{U_\infty}. \tag{2.14}$$

2.2. *Viscously dominated flows ($Re = 0$ and $Re_b \neq 0$)*

We consider the viscous flow past a cylinder in the limit of $Re = 0$, the momentum equation is linear and the two-dimensional vorticity equation is

$$\frac{U_b a}{r} \frac{\partial\omega}{\partial r} = \boldsymbol{\nabla}^2\omega. \tag{2.15}$$

For a two-dimensional flow, the Laplacian reduces to $\boldsymbol{\nabla}_H^2 = \partial^2/\partial r^2 + 1/r\partial/\partial r + 1/r^2\partial^2/\partial\theta^2$. A separable solution to the vorticity equation is sought where $\omega = f(r)\sin\theta$. Substituting into (2.15) we obtain

$$r^2 f''(r) + rf'(r)\left(1 - \frac{U_b a}{\nu}\right) - f(r) = 0. \tag{2.16}$$

This admits a power law solution of the form $f(r) = B(r/a)^\alpha$ where

$$\alpha^2 - \frac{U_b a}{\nu} - 1 = 0, \tag{2.17}$$

or

$$\alpha = \frac{U_b a}{2\nu} - \sqrt{\left(\frac{U_b a}{2\nu}\right)^2 + 1}, \tag{2.18}$$

where the negative root is chosen. Having obtained ω, we must determine the streamfunction, ψ, which satisfies $\boldsymbol{\nabla}_H^2\psi = -\omega$. Again a solution can be constructed which contains contributions from the mean flow and the blow flow:

$$\psi = U_\infty \left(r + \frac{A}{r} + B\left(\frac{r}{a}\right)^{\alpha+2}\right)\sin\theta + U_b a\theta, \tag{2.19}$$

The velocity field is related to the streamfunction through

$$u_\theta = -\frac{\partial\psi}{\partial r}, \qquad u_r = \frac{1}{r}\frac{\partial\psi}{\partial\theta}. \tag{2.20}$$

At $r = a$, we require

$$u_\theta = U_\infty \left(1 - \frac{A}{a} + \frac{B(\alpha + 2)}{a} \right) \sin\theta = 0. \tag{2.21}$$

Therefore

$$A = -\left(\frac{a + 1}{\alpha + 3} \right) a, \quad B = -\frac{2a}{\alpha + 3}. \tag{2.22}$$

From this

$$\omega = -\boldsymbol{\nabla}^2 \psi = -\frac{2U_\infty}{a(\alpha + 3)} \left(\alpha^2 + 3\alpha + 1 \right) \sin\theta \left(\frac{r}{a} \right)^\alpha. \tag{2.23}$$

When $\Lambda < 0$, $\alpha < -1$ so that the mean flow contribution dominates over the contribution from the sucking flow. In the limit of a large sucking flow $|\Lambda| \gg 1$, $\alpha \cong -Re|\Lambda|/2$ and

$$\tilde{\omega} = \frac{2a\omega}{U_\infty} \cong -2Re|\Lambda| \sin\theta \, \tilde{r}^{\frac{1}{2}|\Lambda|Re}. \tag{2.24}$$

The vorticity flux through the top surface of the cylinder is

$$F_\omega = \int_0^\pi a\omega_s U_b \mathrm{d}\theta, \tag{2.25}$$

so that

$$\frac{F_\omega}{U_\infty^2} = 4 \left(\frac{\alpha^2 + 3\alpha + 1}{\alpha + 3} \right). \tag{2.26}$$

For $-\Lambda \gg 1$, the flux is

$$\frac{F_\omega}{U_\infty^2} = 2Re\Lambda^2. \tag{2.27}$$

The analysis is approximate. Oseen approximation. Clearly $\Lambda \to 0$.

For axisymmetric flow past a sphere, te azimuthal vorticity equation in the limit of $Re \ll 1$ is

$$\frac{U_b a^2}{r^2} \frac{\partial \omega_\phi}{\partial r} = \boldsymbol{\nabla}^2 \omega_\phi. \tag{2.28}$$

Dukowicz (1982)† derived an expression for the drag on a rigid sphere for $Re \ll 1$ (from ?) and finite values of ΛRe and showed that the distribution of vorticity through the boundary layer is

$$\tilde{\omega} = \frac{2a\omega}{U_\infty} = -6\tilde{r} \sin\theta \frac{1 - \left(1 + \frac{1}{2}Re\Lambda\frac{1}{\tilde{r}} + \frac{1}{8}Re^2\Lambda^2\frac{1}{\tilde{r}^2} \right) \exp\left(-\frac{1}{2}Re\Lambda\frac{1}{\tilde{r}} \right)}{\left(1 + \frac{1}{2}Re\Lambda \right) \exp\left(-\frac{1}{2}Re\Lambda \right) - 1 + \frac{1}{8}Re^2\Lambda^2}. \tag{2.29}$$

For strongly sucking flow, the vorticity decays exponentially away from the surface and

$$\tilde{\omega} = -\frac{3}{2} \frac{Re|\Lambda|}{\tilde{r}^2} \sin\theta \exp\left(-\frac{1}{2}Re\Lambda \left(\frac{1}{\tilde{r}} - 1 \right) \right), \tag{2.30}$$

which agrees with the boundary layer analysis of (2.52); while for blowing flows

$$\tilde{\omega} = \frac{\frac{Re^3\Lambda^3}{8\tilde{r}^2} \exp\left(-\frac{1}{2}Re\Lambda\frac{1}{\tilde{r}} \right)}{\left(1 + \frac{1}{2}Re\Lambda \right) \exp\left(-\frac{1}{2}Re\Lambda \right) - 1 + \frac{1}{8}Re^2\Lambda^2}. \tag{2.31}$$

† The Reynolds number defined by Dukowicz (1982) is based on the sphere radius, and not the diameter. This is why there are additional factor of 1/2 in the expressions stated in this paper.

The drag coefficient is

$$C_D = 8\Lambda \frac{1 - \left(1 + \frac{1}{2}Re\Lambda\right)\exp\left(-\frac{1}{2}Re\Lambda\right)}{\left(1 + \frac{1}{2}Re\Lambda\right)\exp\left(-\frac{1}{2}Re\Lambda\right) - 1 + \frac{1}{8}Re^2\Lambda^2}. \tag{2.32}$$

For strong sucking flows,

$$C_D \to -8\Lambda, \tag{2.33}$$

which agrees with (2.7). The fraction of the drag force which comes from the viscous stresses is

$$\frac{C_\nu}{C_D} = \frac{4}{Re\Lambda} \frac{1 - \left(1 + \frac{1}{2}Re\Lambda + \frac{1}{8}Re^2\Lambda^2\right)\exp\left(-\frac{1}{2}Re\Lambda\right)}{1 - \left(1 + \frac{1}{2}Re\Lambda\right)\exp\left(-\frac{1}{2}Re\Lambda\right)}, \tag{2.34}$$

which at $\Lambda = 0$ corresponds to a ratio of 2/3 (for $Re \ll 1$). For strongly sucking flows, $C_\nu/C_D = 1$, while for strong blowing flows, $C_\nu/C_D \sim 8/Re\Lambda$. The flux of vorticity from the sphere surface is

$$F_\omega = \int_0^\pi 2\pi a^2 U_b \omega_s \mathrm{d}S. \tag{2.35}$$

or in dimensionless form

$$\frac{F_\omega}{2aU_\infty^2} = \frac{3}{2}\Lambda\pi^2 \frac{1 - \left(1 + \frac{1}{2}Re\Lambda + \frac{1}{8}Re^2\Lambda^2\right)\exp\left(-\frac{1}{2}Re\Lambda\right)}{\left(1 + \frac{1}{2}Re\Lambda\right)\exp\left(-\frac{1}{2}Re\Lambda\right) - 1 + \frac{1}{8}Re\Lambda^2}. \tag{2.36}$$

In the limit of large sucking flows, the vorticity flux is

$$\frac{F_\omega}{2aU_\infty^2} = \frac{3}{8}Re\Lambda^2\pi^2. \tag{2.37}$$

2.3. *Inertially dominated flows* ($Re_b \gg 1$)

We consider the growth of a boundary layer on a rigid body in the limit of $|\Lambda| \gg 1$. For strongly sucking flows, the boundary layer thickness scales as $\delta_\nu \sim \nu/|U_b|$ and as we shall see the flow is ultimately steady on a viscous timescale of T_ν (2.13a). For blowing flows, the boundary layer thickness grows with time as it diffuses and through-surface flow. When $\Lambda \gg 1$, the boundary layer is blown away from the surface and initially $\delta \sim U_b t$ ($\delta \ll a$). When the boundary layer is thin, the momentum equation tangential to the rigid surface for a flat plate ($D = 1$), cylinder ($D = 2$) and sphere ($D = 3$) can be written as

$$\frac{\partial u_s}{\partial t} + U_b \left(\frac{a}{r}\right)^{D-1} \frac{\partial u_s}{\partial r} = \frac{\nu}{r^{D-1}} \frac{\partial}{\partial r}\left(r^{D-1}\frac{\partial u_s}{\partial r}\right), \tag{2.38}$$

where $u_s = \boldsymbol{u} \cdot \hat{\boldsymbol{s}}$. The corresponding momentum equation perpendicular to the boundary layer reduces to

$$0 = \frac{\partial p}{\partial r}, \tag{2.39}$$

so that the pressure is

$$p = p_\infty + \frac{1}{2}\rho U_\infty^2 - \frac{1}{2}\rho|\boldsymbol{\nabla}\phi|^2, \tag{2.40}$$

where p_∞ is the pressure far from the body. The velocity satisfies $u_s = 0$ at $r = a$, for the case of a cylinder and sphere, and $u_\theta = 0$ at $r = 0$ for a flat plate. The boundary layer flow must match the inviscid flow outside the boundary layer $u_s \to \partial\phi/\partial s|_{r=a}$. Non-dimensionalising using $\tilde{u}_s(\tilde{r}, T) = u_s/(\partial\phi/\partial s)_{r=a}$, $T = t/T_\nu$ and $\tilde{r} = r/a$ gives

$$\frac{\partial \tilde{u}_s}{\partial T} = \frac{4}{Re_b^2\Lambda^2} \frac{\partial^2 \tilde{u}_s}{\partial \tilde{r}^2} + \left(\frac{4(D-1)}{\Lambda^2 Re_b^2}\frac{1}{\tilde{r}} - \frac{2}{\Lambda Re_b}\left(\frac{1}{\tilde{r}}\right)^{D-1}\right)\frac{\partial \tilde{u}_s}{\partial \tilde{r}}. \tag{2.41}$$

We first discuss the through-surface flow over a flat wall ($D = 1$) as there is an exact solution. The boundary layer solution that satisfies $\tilde{u}_s(\tilde{r}, 0) = 1$, $\tilde{u}_s(0, T) = 0$ and $\tilde{u}_s(\tilde{r} \to \infty, T) = 1$, is

$$\tilde{u}_s(\tilde{r}, T) = 1 - \frac{1}{2}\mathrm{erfc}\left(\frac{n - U_b t}{\sqrt{4\nu t}}\right) - \frac{1}{2}\exp\left(\frac{U_b n}{\nu}\right)\mathrm{erfc}\left(\frac{n + U_b t}{\sqrt{4\nu t}}\right), \tag{2.42}$$

where $\mathrm{erfc}(z) = 2/\sqrt{\pi}\int_z^\infty \exp(-t^2)\mathrm{d}t$ (Abramowitz & Stegun 1972). The vorticity within the boundary layer is

$$\omega \approx \frac{\partial u_s}{\partial n} = \left[\frac{1}{\sqrt{\pi\nu t}}\exp\left(-\left(\frac{n - U_b t}{\sqrt{4\nu t}}\right)^2\right) - \frac{U_b}{2\nu}\exp\left(\frac{U_b n}{\nu}\right)\mathrm{erfc}\left(\frac{n + U_b t}{\sqrt{4\nu t}}\right)\right]\frac{\partial \phi}{\partial s}\bigg|_{n=0}. \tag{2.43}$$

The circulation across the thin boundary layer,

$$\kappa = \int_0^\infty \omega \mathrm{d}n = \frac{\partial \phi}{\partial s}\bigg|_{n=0}, \tag{2.44}$$

depends only on the velocity outside the boundary layer, regardless of whether the flow is sucking or blowing at least over the period that the boundary layer approximation is valid. The boundary layer circulation corresponds to the circulation per unit length associated with the bound vorticity. The shear stress on the surface is

$$\tau_{sn} = \mu\frac{\partial u_s}{\partial n}\bigg|_{n=0} = -\rho U_b\frac{\partial \phi}{\partial s}\bigg|_{n=0}g(T), \tag{2.45}$$

where

$$g(T) = \frac{1}{2}\mathrm{erfc}\left(\mathrm{sign}(\Lambda)\frac{1}{2}T^{\frac{1}{2}}\right) - \mathrm{sign}(\Lambda)\frac{1}{\pi^{\frac{1}{2}}T^{\frac{1}{2}}}\exp\left(-\frac{T}{4}\right). \tag{2.46}$$

The asymptotic behaviour of the shear stress depends on whether the flow is blowing or sucking. Since $\mathrm{erfc}(z) \sim 2$ as $z \to -\infty$ and $\mathrm{erfc}(z) \sim 2\exp(-z^2)/\sqrt{\pi}z$ as $z \to \infty$. For strong sucking flows ($\Lambda \ll 0$), (2.45) is approximately

$$g(T) \simeq 1 + \frac{1}{\pi^{\frac{1}{2}}T^{\frac{1}{2}}}\exp\left(-\frac{T}{4}\right), \tag{2.47}$$

while for strong blowing flows ($\Lambda \gg 1$), (2.46) is approximately

$$g(T) \simeq \frac{1}{2\pi^{\frac{1}{2}}T^{\frac{1}{2}}}\exp\left(-\frac{T}{4}\right). \tag{2.48}$$

For small T, the boundary layer thickness initially scales as $\delta_\nu/a \sim (t/T_b)^{\frac{1}{2}}$, so that the viscous shear stress decays slowly as as $\rho U_\infty \nu^{1/2}/t^{1/2}$. This analysis does not account for the pressure contribution, which occurs over an advective timescale of T_b (see 2.13). The vorticity in the boundary layer is

$$\tilde{\omega} = Re|\Lambda|\left[\frac{\mathrm{sign}(\Lambda)}{\sqrt{\pi T}}\exp\left(-\left(\frac{n/\delta_\nu - T}{\sqrt{4T}}\right)^2\right) - \frac{1}{2}\exp\left(\frac{n}{\delta_\nu}\right)\mathrm{erfc}\left(\frac{n/\delta_\nu + T}{\sqrt{4T}}\right)\right]\frac{1}{U_\infty}\frac{\partial \phi}{\partial s}\bigg|_{n=0}. \tag{2.49}$$

To illustrate the development of the boundary with time, (2.38) was solved numerically. Figure ? shows the influence of the dimensions of the flow on a developing boundary layer for sucking and blowing flows. For $\Lambda < 0$ the boundary layer velocity tends to a steady state in a short time $\sim T$. For $\Lambda > 0$, the boundary layer is essentially pushed away from the wall where its thickness scales as $\delta_\nu \sim U_b t$. By mass conservation, the

thickness of the boundary layer on a cylinder is $a((1 + 2t/T_b)^{1/2} - 1)$; for short time, the thickness conforms the same as a flat wall, but increases at a slower rate beyond a/U_b, when $\delta_\nu/a \sim (2t/T_b)^{1/2}$. Similarly for a sphere, for short time $\delta_\nu/a \sim t/T_b$, while for longer time $\delta_\nu/a \sim (3t/T_b)^{1/3}$. For blowing flows, the boundary layer analysis breaks down when $\delta_\nu/a \sim (U_b/U_\infty)^{1/(D-1)}$ or $t \sim a/U_\infty$.

For both blowing and sucking flows, the viscous stress is independent of the blow velocity and decays as $1/t^{\frac{1}{2}}$. The reason for this is that the circulation across the boundary layer is independent of the blow velocity for short time.

2.4. *Sucking flow ($\Lambda < 0$)*

We explore in more detail the transient and steady force for strong sucking flow, $-\Lambda \gg 1$, on these rigid bodies. For a sucking flows, the vorticity in the boundary layer of a flat plate ($D = 1$) is

$$\lim_{T \to \infty} \tilde{\omega} = -Re|\Lambda| \exp\left(-\frac{|\Lambda|Rey}{2a}\right). \tag{2.50}$$

For $\delta_\nu/a \ll 1$, the unsteady boundary layer analysis for the flat plate provides a leading order description of the boundary layer structure on a cylinder and sphere. Specifically for a sucking flow, the distribution of vorticity in the boundary layer is

$$\lim_{T \to \infty} \tilde{\omega} = -2Re|\Lambda|\tilde{r}^{-\frac{1}{2}|\Lambda|Re} \sin\theta, \tag{2.51}$$

while for a sphere,

$$\lim_{T \to \infty} \tilde{\omega} = -\frac{3}{2\tilde{r}^2} Re|\Lambda| \exp\left(-\frac{1}{2}|\Lambda|Re(\tilde{r} - 1)\right) \sin\theta. \tag{2.52}$$

Expression (2.52) is the same as (2.30).

When $|\Lambda|Re \gg 1$, the vorticity profiles for a cylinder and sphere (2.51) and (2.52) tend to the flat plate solution (2.50) because the boundary layer becomes much thinner than the size of the body. (When $|\Lambda| \gg 1$, $\tilde{r}^{-\frac{1}{2}|\Lambda|Re} = (1 + (\tilde{r}-1))^{-\frac{1}{2}|\Lambda|Re} \to \exp(-\frac{1}{2}|\Lambda|Re(\tilde{r}-1))$).

The flux of vorticity through the surface can be calculated using (2.51) and (2.52) to give

$$\frac{F_\omega}{U_\infty^2} = 2Re\Lambda^2, \qquad \frac{F_\omega}{2U_\infty^2 a} = \frac{3}{8}\pi^2 Re\Lambda^2 \tag{2.53}$$

for a cylinder and a sphere respectively.

The pressure gradient normal to the boundary layer is small and the surface pressure (from (2.40)) corresponds to the irrotational solution, which for a cylinder is

$$C_P \equiv \frac{p - p_\infty}{\frac{1}{2}\rho U_\infty^2} = 1 - 4\sin^2\theta - \Lambda^2, \tag{2.54}$$

and a sphere is

$$C_P = 1 - \frac{9}{4}\sin^2\theta - \Lambda^2. \tag{2.55}$$

The force on the body can be evaluated from (?). As we see above, the pressure distribution corresponds to the potential flow prediction and does not contribute to a total force on the body. From (?), the viscous component of the drag force is

$$F_\nu = \int_{S_B} \tau_{ns} n_y \mathrm{d}S = -\rho U_b \left(\int_{S_B} \left.\frac{\partial\phi}{\partial s}\right|_{r \to a} n_y \mathrm{d}S\right) g(T), \tag{2.56}$$
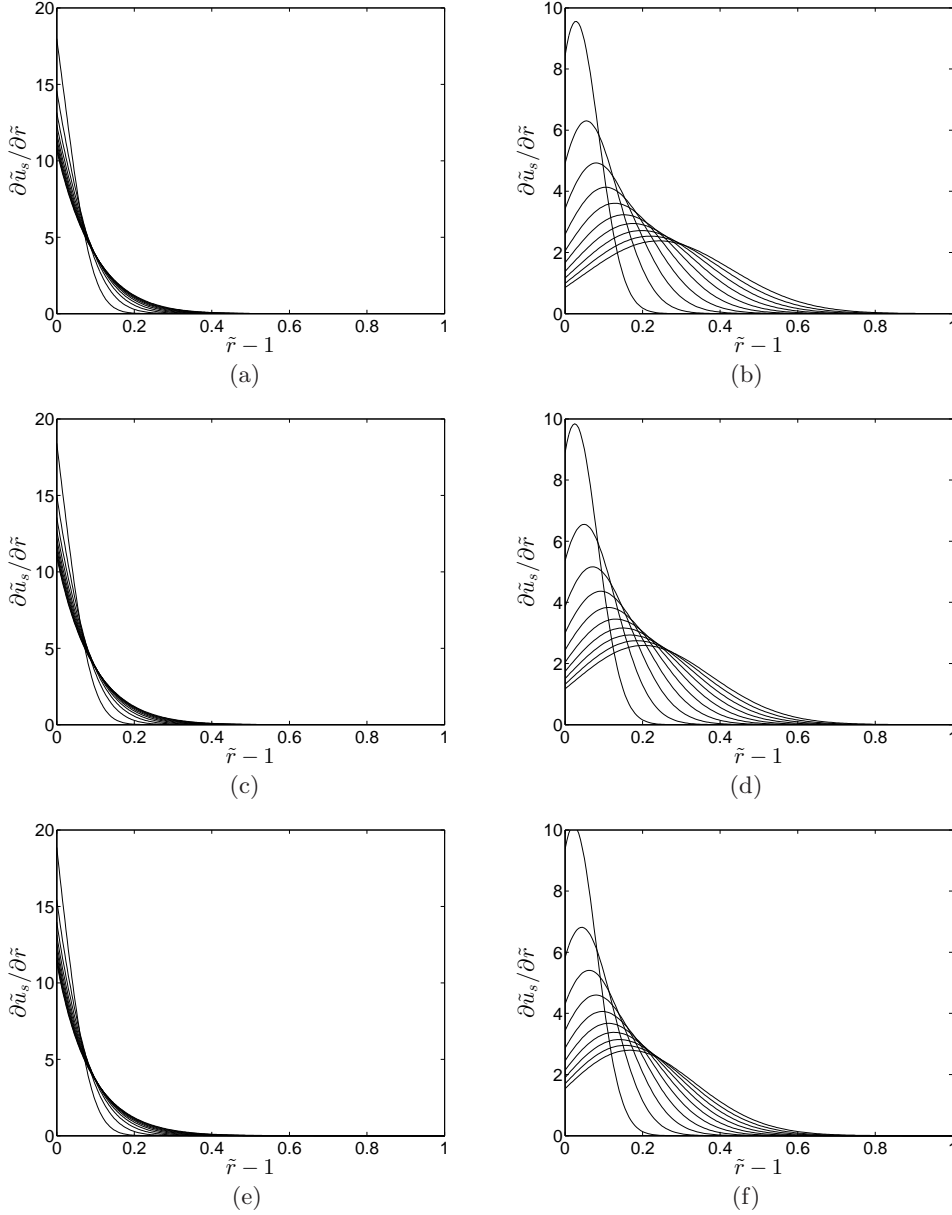
Figure 2: Time sequence of the boundary layer flow for (*a*) flat plate ($D = 1$), (*b*) cylinder ($D = 2$) and (*c*) sphere ($D = 3$). On the left-hand side the flow is sucking ($\Lambda = -1$, $Re = 10$) and the right-hand side there is a blowing flow ($\Lambda = 1$, $Re = 10$). The calculations are run up to time $Re/5$.

and can be evaluated explicitly to show that the viscous component is

$$F_\nu = -2\pi a \rho U_\infty U_b g(T), \qquad -4\pi a^2 \rho U_\infty U_b g(T). \tag{2.57}$$

For large time, the drag force tends to a constant,

$$F_D = -\rho U_\infty Q_s, \tag{2.58}$$

which agrees with (2.7). More specifically, the steady drag coefficients are

$$C_D = -\Lambda \quad (D=1), \qquad -2\pi\Lambda \quad (D=2), \qquad -8\Lambda \quad (D=3), \qquad (2.59)$$

where

$$C_\nu/C_D = 1, \qquad (2.60)$$

since the drag associated with the pressure component is zero. The estimates (2.59) are valid providing the boundary layer is thin, *i.e.* $\nu/|U_b| < 0.1a$ or $|\Lambda| > 10/Re$. A more general proof of (2.58) from (2.56) for two-dimensional bodies symmetric about the x-axis or axisymmetric bodies is given in Appendix A. When the flow symmetry is broken, the body may also experience a lift force.

In the limit of $-\Lambda \gg 1$, the flow outside the boundary layer is irrotational and large gradients in the flow are confined to the boundary layer. This is a special case when the total dissipation in the entire body of fluid is finite and the energy equation can be applied to estimate the drag force. This technique is well-known in the context of Levich's (1949) estimate of the drag on a clean bubble (see Moore 1963, Stone 1992). From Landau & Lipshitz (1965, p. 50), the unsteady form of the energy equation (in the frame of reference with the fluid at infinity at rest) is

$$\int_{V-V_B} \frac{\partial}{\partial t} \frac{1}{2}\rho u^2 \mathrm{d}V = \int_{S_B+S_\infty} \left(-\boldsymbol{u}\left(p+\frac{1}{2}\rho u^2\right) + \boldsymbol{u}\cdot\boldsymbol{\tau}\right)\cdot\hat{\boldsymbol{n}}\mathrm{d}S - \epsilon, \qquad (2.61)$$

where S_B is the surface of the body and S_∞ is a control surface far from the body. The viscous dissipation term ϵ is defined by

$$\epsilon = \frac{1}{2\mu}\int_{V-V_B} \boldsymbol{\tau}:\boldsymbol{\tau}\mathrm{d}V \left(\equiv \int_{V-V_B} \boldsymbol{\tau}:\boldsymbol{\nabla}\boldsymbol{u}\mathrm{d}V \right), \qquad (2.62)$$

and is evaluated over the whole flow domain (V) excluding the body (V_B). To evaluate the drag force, we must evaluated (2.61) in the frame of reference with the ambient flow at rest and the body moving.

In the far field the flow is irrotational, so that $p + \frac{1}{2}\rho u^2 = p_0 - \rho\partial\phi/\partial t$ and the viscous stresses are weak in the far field. Therefore the contribution from the integral over S_∞ reduces to

$$\int_{S_\infty} p_0\boldsymbol{v}\cdot\hat{\boldsymbol{n}}\mathrm{d}S = \int_{S_B} U_b p_0\mathrm{d}S, \qquad (2.63)$$

since the flux from the surface of the body is independent of the shape of S_∞. In addition, since the body moves with a constant velocity and the flow is steady in the moving frame, the left-hand side of (2.61) is

$$\int_{V-V_B} \frac{\partial}{\partial t}\frac{1}{2}\rho u^2\mathrm{d}V = \int_{V-V_B} v_i \frac{\partial}{\partial x_i}\frac{1}{2}\rho u^2\mathrm{d}V = \int_{S_B} \boldsymbol{v}\cdot\hat{\boldsymbol{n}}\frac{1}{2}\rho u^2\mathrm{d}S. \qquad (2.64)$$

Under these conditions, the right-hand side of (2.61) can be recast in terms of

$$\boldsymbol{v}\cdot\boldsymbol{F} = \int_{S_B} \boldsymbol{v}\cdot(p\boldsymbol{I}-\boldsymbol{\tau})\cdot\hat{\boldsymbol{n}}\mathrm{d}S. \qquad (2.65)$$

Expressing the viscous stress as $\boldsymbol{\tau} = \tau_n\hat{\boldsymbol{n}} + \tau_s\hat{\boldsymbol{s}}$ and using the boundary condition (2.1,2.2), we can rewrite (2.61) in a general form:

$$F_D U_\infty \equiv \epsilon + \int_{S_B} U_b\left(p+\frac{1}{2}\rho u^2 - p_0 - \tau_n\right)\mathrm{d}S - \int_{S_B} (\boldsymbol{u}-\boldsymbol{v})\cdot\boldsymbol{v}\tau_s\mathrm{d}S. \qquad (2.66)$$

For a clean bubble the tangential shear stress is zero ($\tau_s = 0$) and $U_b = 0$, we retrieve

Levich's result that $F_D = \epsilon/U_\infty$ for a clean non-blowing bubbles. In our case, there is no tangential slip velocity and the last term is zero. This provides a scaling analysis to estimate the relative configuration to drag from the boundary layer and the region outside. The coefficient can be determined from an analysis of the boundary layer structure. We can estimate the various terms on the right-hand side for the case of a cylinder and sphere, using the boundary layer analysis for the velocity field.

For a cylinder, the boundary layer flow (in the frame in which the far field is at rest) is

$$u_\theta = \frac{U_\infty a^2}{r^2} \sin\theta \left(1 - 2e^{(r-a)U_b/\nu}\right), \quad u_r = \frac{U_\infty a^2}{r^2} \cos\theta + \frac{U_b a}{r}. \tag{2.67}$$

The dissipation term,

$$\epsilon = \int_{V-V_B} \left[2\mu \left(\left(\frac{\partial u_r}{\partial r}\right)^2 + \left(\frac{1}{r}\frac{\partial u_\theta}{\partial \theta} + \frac{u_r}{r}\right)^2 \right) + \mu \left(r\frac{\partial}{\partial r}\left(\frac{u_\theta}{r}\right) + \frac{1}{r}\frac{\partial u_r}{\partial \theta} \right)^2 \right] \mathrm{d}V, \tag{2.68}$$

can be evaluated analytically by substituting

$$\epsilon = 12\pi U_\infty^2 \mu - 64\pi U_\infty^2 \mu \int_0^\infty \left(\frac{1}{(1+z)^5} - \frac{U_b a/4\nu}{(1+z)^4} \right) \exp\left(\frac{U_b az}{\nu}\right) \mathrm{d}z$$

$$-\frac{4\pi U_\infty^2 U_b^2 \rho a^2}{\nu} \int_0^\infty \left(\frac{1}{(1+z)^3} + \frac{6\nu/U_b a}{(1+z)^4} - \frac{11\nu^2/a^2 U_b^2}{(1+z)^5} \right) \exp\left(\frac{2U_b az}{\nu}\right) \mathrm{d}z. \tag{2.69}$$

In the limit of $Re|\Lambda| < 10$, the exponential terms decay sufficiently rapidly that the dissipation can be integrated

$$\epsilon \cong -2\pi\rho a U_b U_\infty^2 \left(1 - \frac{16}{Re\Lambda} + \frac{84}{Re^2\Lambda^2} \right). \tag{2.70}$$

The integral of the normal viscous stress over the surface of the cylinder is

$$\int_{S_B} \tau_n \mathrm{d}S \cong -2\pi U_b \mu. \tag{2.71}$$

As we have already discussed, the irrotational flow outside the boundary layer determines the pressure field at the cylinder surface and since the velocity normal to the cylinder surface is continuous,

$$p + \frac{1}{2}\rho u^2 - p_0 = \frac{1}{2}\rho(U_\infty^2 \sin^2\theta - u_\theta^2) - p_0 = 0, \tag{2.72}$$

because the tangential velocity is reversed in sign across the boundary layer. Combined together, we find for a cylinder

$$F_D \cong (\epsilon - U_b \int_{S_B} \tau_n \mathrm{d}S)/U_\infty \cong -2\pi a\rho U_b U_\infty \left(1 - \frac{16}{Re\Lambda} + \frac{84}{Re^2\Lambda^2} - \frac{2\Lambda}{Re} \right). \tag{2.73}$$

To leading order, the rate at which work is done by the force on the cylinder is balanced by dissipation because the energy flux due to the sucking flow is small. The largest correction is due to dissipation caused by the blowing flow and the normal viscous stresses. These cause the drag to be larger by a factor $1/Re|\Lambda|$ than that accounted for in the boundary layer analysis.

For flow past a sphere, the boundary layer flow (in the frame in which the far field is at rest) is

$$u_\theta = \frac{U_\infty a^3}{2r^3} \sin\theta \left(1 - 3e^{(r-a)U_b/\nu}\right), \quad u_r = \frac{U_\infty a^3}{r^3} \cos\theta + \frac{U_b a^2}{r^2}. \tag{2.74}$$

For axisymmetric flows the dissipation term is,

$$\epsilon = \int_{V-V_B} \left[2\mu \left(\left(\frac{\partial u_r}{\partial r} \right)^2 + \left(\frac{1}{r}\frac{\partial u_\theta}{\partial \theta} + \frac{u_r}{r} \right)^2 \right) + \mu \left(r\frac{\partial}{\partial r}\left(\frac{u_\theta}{r} \right) + \frac{1}{r}\frac{\partial u_r}{\partial \theta} \right)^2 + 2\mu \left(\frac{u_r}{r} + \frac{u_\theta}{r}\cot\theta \right)^2 \right] dV,$$

(2.75)

$$= 28\pi U_\infty^2 \mu a + 108\pi\mu a U_\infty^2 \int_0^\infty \left(\frac{1}{(1+z)^6} + \frac{4U_b a/9\nu}{(1+z)^6} - \frac{6U_b^2 a^2/108\nu^2}{(1+z)^5} \right) \exp\left(\frac{2U_b az}{\nu} \right) dz$$

(2.76)

$$+ 120\pi\mu U_\infty^2 a \int_0^\infty \frac{(1+U_b a/5\nu)}{(1+z)^6} \exp\left(\frac{2U_b az}{\nu} \right) dz.$$

This can be evaluated to give

$$\epsilon \cong -3\pi a^2 U_b U_\infty^2 \rho \left(1 - \frac{32}{Re\Lambda} - \frac{152}{Re^2\Lambda^2} \right)$$

(2.77)

Now, on the surface of the sphere

$$p + \frac{1}{2}\rho u^2 - p_0 = \frac{1}{2}\rho(U_\infty^2 \sin^2\theta - u_\theta^2) - p_0 = \frac{3}{8}\rho U_\infty^2 \sin^2\theta,$$

(2.78)

so the integral over the surface is $\rho\pi a^2 U_\infty^2 U_b$. The viscous stress term is

$$\int_{S_B} \tau_n dS \cong -8\pi U_b \mu a.$$

(2.79)

In total, we

$$F_D \cong \left(\epsilon - \rho\pi a^2 U_b U_\infty -_{S_B} \tau_n dS \right) /U_\infty \cong -4\pi a^2 U_b U_\infty \rho \left(1 - \frac{24}{Re\Lambda} - \frac{114}{Re^2\Lambda^2} - \frac{4\Lambda}{Re} \right).$$

(2.80)

This agrees with (2.7). In this case, dissipation only accounts for 75% of the total drag force with 25% due to the flux of energy due to the sucking flow through the sphere's surface.

2.5. *Blowing flows*

For a large blow velocity, we expect the vorticity to form detached shear layers that bear a similarity to the shear layers that occur in other types of flows, for instance, flows past groups of bodies (Nicolle & Eames 2011) or porous sheets (Castro 1971). Typically, at some distance downstream, the shear layers become unstable and generate a von Kármán vortex street. During the initial phase, the vortex sheets are well separated and the decay in the maximum vorticity is extremely slow. Depending on whether the Reynolds number of the flow is sufficiently low, the transition to a faster rate of decay is likely not to be observed since it requires the vorticity in adjacent vortex lumps to merge and decay by diffusion. For example, for $\Lambda = 0$, this transition is observable at a distance of $O(aRe)$, which is usually too far downstream to observe at even moderate Re.

The downstream signature is intrinsically linked to the forces acting the body. Insight can be gained by analysing the viscous and pressure contribution to the force on the body. For the case of a cylinder, the tangential momentum equation

$$\frac{1}{a}\frac{\partial}{\partial\theta}\left(p + \frac{1}{2}\rho u^2 \right) = -\rho U_b \omega_s + \mu \left(\frac{\omega_s}{a} + \frac{\partial\omega}{\partial r} \right).$$

(2.81)

In the limit of a large blow velocity, we expect physically that the velocity gradients near

the surface are diminished due to the boundary layer being removed. In this limit, we expect the drag to be dominated by pressure so that $\omega_s \sim 1/U_b$. An alternative argument can be developed from the wake flows. On integration this yields

$$p = -\frac{1}{2}\rho U_b^2 - \left(\rho a U_b - \frac{\mu}{a}\right) \int_0^\theta \omega_s \mathrm{d}\theta + \mu \int_0^\theta \frac{\partial \omega}{\partial r} \mathrm{d}\theta. \tag{2.82}$$

Since we expect $C_p + \Lambda^2$ to be unity at the front stagnation point, we can non-dimensionalise (2.53) to give

$$C_p + \Lambda^2 = 1 - \Lambda \int_{-\pi}^\theta \tilde{\omega}_s \mathrm{d}\theta. \tag{2.83}$$

The drag force is estimated as

$$C_D = -\frac{\Lambda}{A_{XS}} \int_{S_B} n_x \int_{-\pi}^\theta \tilde{\omega}_s \mathrm{d}\theta \mathrm{d}A. \tag{2.84}$$

The drag force on the cylinder is dominated by pressure variation and scales as $U_b \omega_s \rho a$; as we shall see later, the drag force is weakly dependence on U_b giving

$$\omega_s \sim \frac{U_\infty^2}{2aU_b}. \tag{2.85}$$

The distribution of vorticity in the far field is connected with how it is introduced into the flow. Although the flow will be unsteady far downstream, a steady analysis can identify some of the critical physics of the wake flow and its connection with the near field. Focussing on the two-dimensional case in the limit of $\Lambda \gg 1$, the flow induced by the vortical component of the flow is weak and the vorticity is advected by the irrotational flow.

To understand this process, we analyse the flux of vorticity from the cylinder surface. For a blowing flow ($\Lambda > 0$) since $\omega_s \sim U_\infty^2/2aU_b$ then the vorticity flux is weakly dependant on the blow velocity,

$$\frac{F_\omega}{U_\infty^2} \cong -1. \tag{2.86}$$

Prior to the shear layers becoming unstable, the flux of positive vorticity along the streamline is conserved because the cancellation in two-dimensions can only come from annihilation by combining positive and negative vorticity (Hunt & Eames 2002). The properties of the shear layer can be explored by considering the diffusion of a thin vortex sheet. A local similarity solution for the vorticity field across the shear layer is

$$\omega = \omega_m \exp\left(-\frac{n^2}{2Y_\delta^2}\right), \tag{2.87}$$

where ω_m is the maximum vorticity and Y_δ the thickness of the local shear layer. ω_m and Y_δ are functions of s. The flux of vorticity along a shear layer is conserved, so that

$$F_\omega = \int_{-\infty}^\infty u_s \omega \mathrm{d}n = \sqrt{2\pi} \omega_m u_s Y_\delta, \tag{2.88}$$

is constant where u_s is the tangential velocity along the streamline that corresponds to the maximum vorticity. The width of the vortex sheet grows due to diffusion, *i.e.*

$$\frac{1}{2} u_s \frac{\mathrm{d}Y_\delta^2}{\mathrm{d}s} = \nu. \tag{2.89}$$

Combining (2.88) and (2.89) we obtain a relationship between

$$\left[\left(\frac{U_\infty}{\omega_m a}\right)^2\right]_0^s = \frac{8\pi}{Re}\tilde{u}_s^2 \frac{1}{F_\omega^2}\int_0^s \frac{\mathrm{d}\tilde{s}}{\tilde{u}_s}, \qquad (2.90)$$

where $\tilde{s} = s/a$ and $\tilde{u}_s = u_s/U_\infty$. The argument is similar for the shear layers detaching from a sphere, with $F_\omega/2aU_\infty^2 \cong -1$. The distance of the vortex sheet from the centreline must be taken into account, so that the vorticity flux is

$$F_\omega = \int_{-\infty}^\infty u_s\omega_m Y_w \exp\left(-\frac{n^2}{2Y_\delta^2}\right)\mathrm{d}n \qquad (2.91)$$

Rearranging, then

$$\left(\frac{F_\omega}{U_\infty\omega_m Y_w a}\right)^2 = \frac{8\pi}{Re}\frac{u_s}{U_\infty}\int \frac{\mathrm{d}s/a}{u_s/U_\infty}. \qquad (2.92)$$

The effect of a blow flow is to displace the boundary layer away from the surface of the body.

3. Numerical formulation

To understand the coupled effect of inertial and viscous forces on through surface flows, a series of numerical calculations were undertaken for $Re = 1$ to 100 and $-3 \leq \Lambda \leq 3$. Both the two-dimensional flow past a rigid cylinder and axisymmetric flow past a sphere were considered.

3.1. *Geometry, solver and validation*

Figure 3 shows a schematic of the finite computational domain, which for the two-dimensional problem has width $2W$ and length $2L$; for an axisymmetric flow the domain radius was was W. We chose $W/a = 500$ and $L/a = 200$. The challenge is that the force calculations are sensitive to the finite size of the computation domain. The sensitivity is related to the fact that the boundary conditions imposed on the computational domain are $U_\infty\hat{\boldsymbol{x}}$ on the inlet surface, kinematic and no-slip condition on the rigid cylinder, zero flux on the sidewalls and a constant pressure contraint on the outlet. In addition to making the domain large, the boundary layer is extremely thin for the case of strong sucking. Since the boundary layer scales as $\nu/|U_b|$ (for $\Lambda < 0$) and typically 10 points are used to resolve these scales, the smallest elements were of thickness $h/a \sim 0.1/|Re_b|\Lambda$, which for $Re = 100$ and $\Lambda = 3$, gives elements which have sides of length $0.0003a$. For a blowing flow, the boundary layer is much thickner and elements of the size of $0.003a$ where found to be sufficient. The computational domain in the vicinity of the cylinder and sphere were refined in two circular regions (R_3 and R_4) of radius $5a$ and $1.2a$. The domain was meshed using Gmsh (Geuzaine & Remacle 2009).

The momentum and continuity equations were solved using ACEsim (www.acesim.co.uk) which is a general finite element code employing a characteristic based split formulation (Zienkiewicz, Taylor & Nithiarasu 2005). The defining equations are solved in 3 steps: involving first the calculation of an intermediate velocity field using the forcing by the viscous forces. The next step is the calculation of the pressure field, from the fact that the Laplacian of pressure is proportional to the divergence of the intermediate velocity. The pressure is applied to force the intermediate velocity field to be solenoidal, and the updated velocity field is calculated in the third step (Nicolle & Eames 2011). The code has been validate for two-dimensional flows by Nicolle & Eames (2010). An axisymmetric
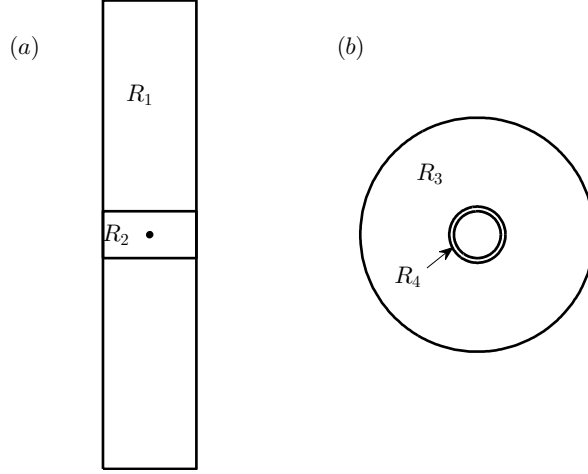
Figure 3: (*a*) Schematic of the computational domain used for the planar flow calculation; for axisymmetric flow, the domain is cut in half through the cylinder. The domain has a width $2W$ and length $2L$, where $W = 500a$ and $L = 200a$. In (*b*), the two circular regions of inner and outer radius (denoted by R_3 and R_4), radius $5a$ and $1.2a$, concentric to the cylinder are shown. For the blowing case, mesh size is $0.0075a$ in region R_4, growing to $0.1a$ on the outer circle. For a sucking flow, mesh size is $0.005a$ in region R_4, growing to $0.02a$ in the outer circle.

formulation was developed and applied in this paper and the computational steps are listed in the Appendix B.

3.2. *Effect of boundedness on drag force*

Flow boundedness has a significant influence on the drag calculations. We first discuss the influence of a domain $2W$ long and $2L$ wide on the two-dimensional calculations. On the inlet of the computational domain, a uniform flow of speed U_∞ is applied. For a sucking flow, the bounding side walls generate a symmetric flow perturbation to the flow in the vicinity of the cylinder, which has a negligible effect on the drag force. As a consequence of the finite length of the domain, a streamwise flow perturbation is generated in the vicinity of the cylinder. This perturbation (ΔU), can be estimated using the method of images to account for the kinematic effect of the channel walls and the inlet condition, to give

$$\Delta U = \sum_{k=0,\pm1,\pm2,\dots} \left(\frac{\pi U_b a W}{W^2 + L^2 k^2} \right) = \frac{a\pi U_b}{W} \left(1 + \frac{W\pi}{L} \coth \frac{W\pi}{L} \right). \qquad (3.1)$$

The cylinder 'sees' an effective streamwise flow $U_\infty + \Delta U$. So for $\Lambda < 0$, the drag on a cylinder is

$$F_D = -2\pi \rho U_b a \left(U_\infty + \Delta U \right). \qquad (3.2)$$

The drag coefficient in an bounded flow C_D is related to an unbounded flow C_{D_∞}, for a sucking flow, through,

$$C_D = C_{D_\infty} \left(1 + \frac{a\pi\Lambda}{W} \left(1 + \frac{W\pi}{L} \coth \frac{W\pi}{L} \right) \right). \qquad (3.3)$$

When the domain is wide (eg $L/W \gg 1$), the correction to the drag is $a\pi^2\Lambda/L$ (about 30% of this comes from the nearest image source term). For example, a sucking flow $\Lambda = -3$, where $L/a = 200$, we expect that the numerical calculations to give a drag coefficients 15% lower than the unbounded estimates. This technique can be used to correct the vorticity distribution on the surface of the cylinder.

For a blowing flow, we anticipate that $F_{D_\infty} \sim \rho C_{D_\infty} U_\infty^2$ where C_{D_∞} has a weak dependence on U_b. In this case, $C_D \sim C_{D_\infty}(1 + \Delta U/U_\infty)^2$ and the effect of flow boundedness leads to the drag coefficient being over predicted by 30% for $\Lambda = 3$. It is so strong that it changes the reported trend that C_D decreases with Λ for cylinders (see later).

For axisymmetric (or three-dimensional) flow through a pipe of radius L, a similar argument point source calculation can be applied. In this case, we anticipate $\Delta U \sim a^2 U_b^2/L^2$ and decays so quickly with L that we expect that its influence on the drag coefficient to be negligible.

4. Unsteady forces

4.1. *Cylinder*

Figure 4 shows the variation of the drag coefficient with time for $Re = 1$. The blue symbols represent the case of blowing and the red symbols sucking. Both C_P and C_D are plotted as functions of time and confirm that the drag force shows an initial weak dependence on the Λ. As expected, the pressure component forms a large fraction of the total drag force. For the case of $\Lambda < 0$, we see the viscous force decays as $t^{-1/2}$ and tends to a steady state in a time scale $\sim T_\nu$. For $\Lambda > 0$, we see that the drag coefficient initially decreases as $t^{-1/2}$, for later time.

Figure 5 shows the results for $Re = 100$. The scalings for $\Lambda > 0$ and < 0 are sufficiently different, that the drag coefficients are plotted separatel; for comparison the result for $\Lambda = 0$ are included. The calculations for $\Lambda < 0$ are run with a finer mesh to capture the thin boundary layer and this results in a smaller time-step than for $\Lambda > 0$. Both figure 5(a,b) confirm that for short time, the drag coefficient decays as $t^{-1/2}$ weakly dependent on the blow velocity. For $\Lambda < 0$, C_D has tended to a constant in a time $\sim T_a$; it appears that there is only one critical time scale. For $\Lambda > 0$, it appears clear that there are multiple timescales. The normalised viscous component of the force is plotted against time in figure 5(c,d) on linear and logarithmic scales. There is good agreement with (2.50) confirming that the viscous force scales as $2\pi a\rho|U_b|U_\infty$ and that this component decays over a timescale of T_ν. Figure 4(d) shows that the while the viscous component as an initial $t^{-1/2}$ dependence, the later decay is exponential for the blowing case, up to when the viscous boundary layer becomes thick and advection between important. The pressure component to the total force is more difficult to interprete largely because the blowing advective timescale is comparable to the advective timescale.

4.2. *Sphere*

The results for the axisymmetric flow past a sphere with a through-surface flow, mirrors closely observations for a cylinder. For $Re = 1$, the majority of the force has a viscous component with both the viscous and pressure components decaying as $1/t^{1/2}$. The pressure component in this case is initially less than $1/3$ the total drag force.
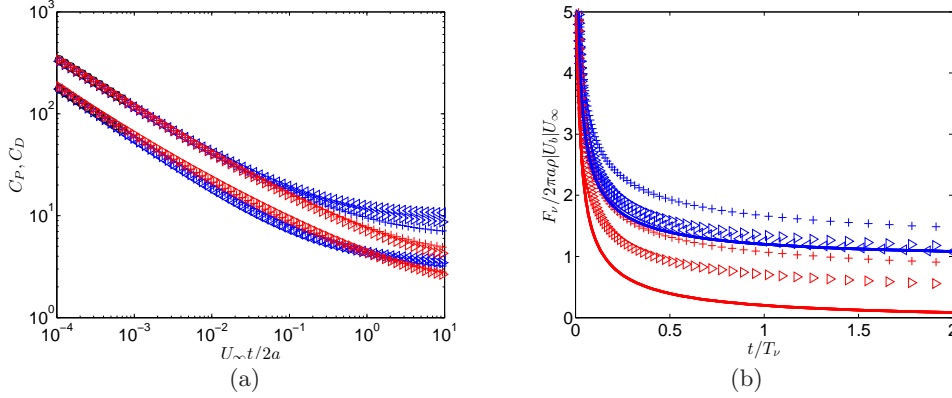
Figure 4: The characteristics of the drag force on a cylinder at $Re = 1$ and $\Lambda = -3, -2, -1, 0, 1, 2$ and 3. In (a), both the pressure coefficient (C_P) and drag coefficient (C_D) are plotted as functions of t, where t is normalised by the advective timescale. In (b), the viscous component for the force (for non-zero values of Λ) are plotted as a function of t, normalised by the viscous blow timescale. The red / blue symbols correspond to $\Lambda > 0$ / < 0 respectively.

Figure 7 shows the variation of the total drag coefficient for a sphere at $Re = 100$. Over a timescale of $\sim T_\nu$ the drag on a sphere for $\Lambda < 0$ quickly decays to a steady state and the initial decrease is $t^{-1/2}$, in a similar manner to the cylinder. As with the case of the cylinder the initial development of the boundary layer structure largely explains the initial decrease of the viscous component of the force. The pressure component to the total force for $\Lambda < 0$ is negligible and forms less than 2% of the total force. For $\Lambda > 0$, the pressure component partially collapses for intermediate values of t/T_b up to $5T_b$, after which the decay for strong blowing decreasing as $t^{1/6}$ before asymptoting to a constant value.

5. Steady forces

5.1. *Cylinder*

The steady drag coefficient for $|\Lambda| \leq 3$ are shown in figure 8(a) for $Re = 1, 10$ and 100; the fraction of the total force which is due to viscous stresses is shown in figure 8(b). This shows that the drag force tends to increase as Λ decreases owing the increase in the viscous stresses on the surface of the cylinder. For $Re = 1$, the variation of the viscous component with Λ is 30% over the range of Λ considered, with $C_\nu/C_D = 1/2$.

The influence of the sucking flow has a dramatic effect on the drag coefficient, as shown in figure ??(a). For $Re = 10, 100$, the drag coefficient shows an approximately linearly increase with Λ, in accordance with (2.59). For a blowing flow, the numerical results show that the drag coefficient has a weak dependence on Λ, with a small tendancy of C_D to increase with Λ. The drag coefficient corrected for flow boundedness is shown for a cylinder and $Re = 100$ in figure 9. It is clear that the correction is important even through the flow domain is extremely large, tending to raise the drag coefficient for $\Lambda < 0$. In addition, correcting for flow boundedness means that the increase of C_D is not evident for $\Lambda > 0$; a trend which is consistent with observations for the sphere.

At higher Re, the drag force largely dominated by viscous forces for $\Lambda < 0$ and pressure forces for $\Lambda > 0$, consistent the mathematical model.
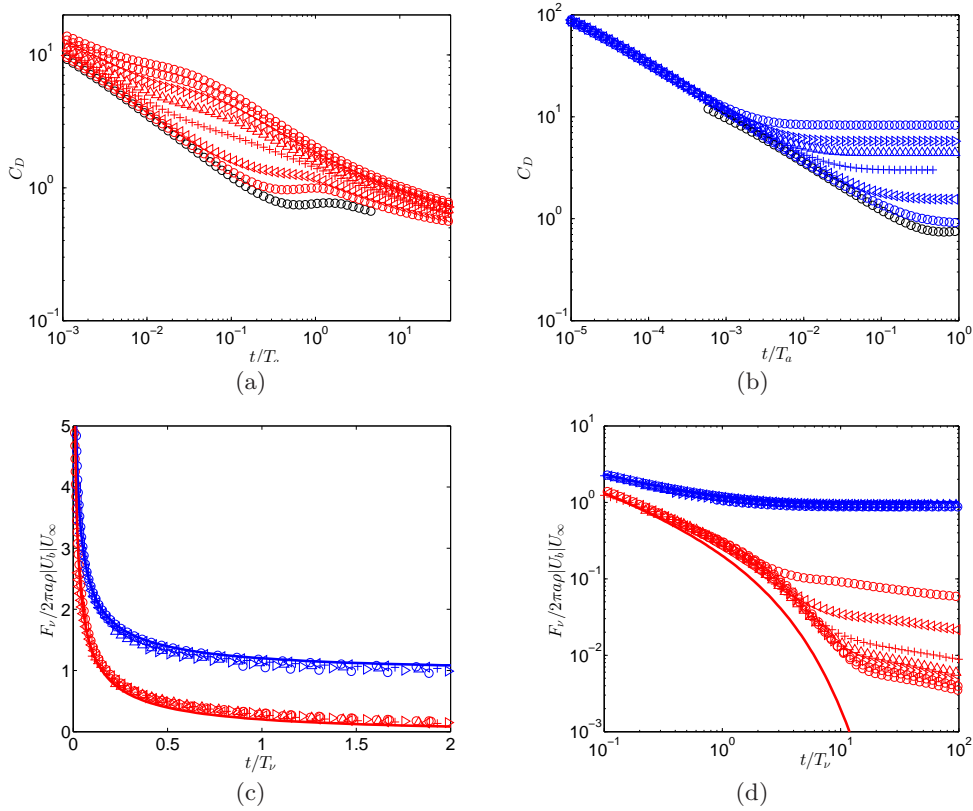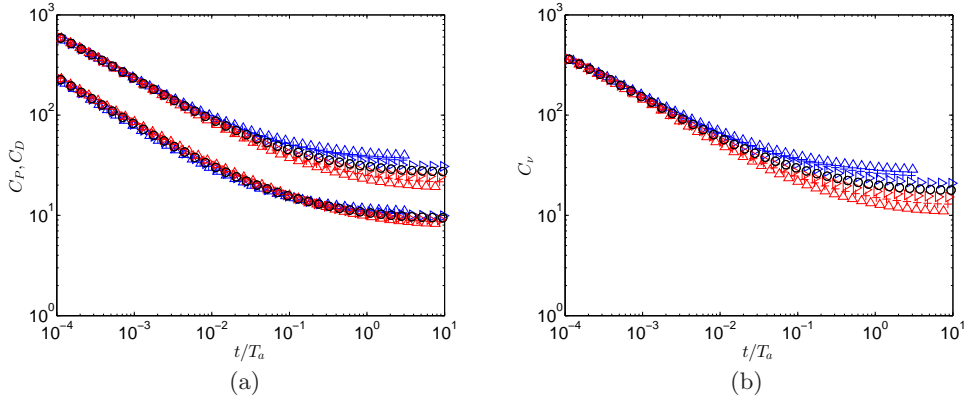
Figure 5: The characteristics of the drag force on a cylinder at $Re = 100$ and $\Lambda = -3, -2, -1, 0, 1, 2$ and 3. In (a,b) the drag coefficient is show as a function of t, normalised by the advective timescale, for $\Lambda > 0$ and < 0 respectively. The viscous component of the drag force is plotted in (c,d); to highlight the different decay rates (for long and short time), the viscous force is plotted on a linear scale in (c) and logarithmic scale in (d).

5.2. *Sphere*

The steady drag coefficient for $|\Lambda| \leq 3$ is shown in figure 8(c) for $Re = 1, 10$ and 100; the fraction of the total force which is due to viscous stresses is shown in figure 8(d). The influence of flow boundedness is negligible for a sphere, which explains the excellent agreement between calculations and predictions for $Re = 100$ and the linear increase of the drag coefficient with Λ. The results for the drag coefficient for $Re = 1$ agree with the curve from Lever & Weber (1985); the theoretical prediction by Dukowicz (1981); the results of Baghchi (2007) for $Re = 100$ are also plotted. For large Λ, we find that $C_D \approx 0.538$.

The fraction of the drag force which arises from viscous stresses is shown in figure 8(d). For $Re = 1$, the viscous force is approximately $2/3$ of the total force. At higher Re, the drag force largely dominated by viscous forces for $\Lambda < 0$ and pressure forces for $\Lambda > 0$, consistent the mathematical model. The theoretical prediction (2.34) for C_ν/C_D by Dukowicz (1981) agrees with the numerical results for $Re = 0.1$; the agreement for higher values of Re seems fortuitous because the drag coefficient is under predicted by his Stokes model.

(a)   (b)

Figure 6: The characteristics of the drag force on a sphere at $Re = 1$ and $\Lambda = -3, -2, -1, 0, 1, 2$ and 3. In (a), both the pressure coefficient (C_P) and drag coefficient (C_D) are plotted as functions of t, where t is normalised by the advective timescale. In (b), the viscous component for the force (for non-zero values of Λ) are plotted as a function of t, normalised by the viscous blow timescale. The red / blue symbols correspond to $\Lambda > 0$ / < 0 respectively.

6. Boundary layer structure

6.1. *Vorticity field*

6.1.1. *Cylinder*

The boundary layer structure of the vorticity field for a cylinder is shown in figure 10 for $Re = 1$. A sucking flow increases the rate at which vorticity decays from the cylinder and also increase the magnitude on the surface of the cylinder; blowing generates the opposite trend.

At higher Re, the influence of advection becomes much more pronounced. Figure 11(a, b) shows the vorticity distribution for $Re = 100$ along the line $\theta = 90^o$ and $\Lambda = 1, 2, 3$. The scalings serve to demonstrate that the surface vorticity decreases as $1/|\Lambda|$ and has a lateral extend which increases with Λ. In contrast, for a sucking flow, we find that the vorticity on the surface scales as $Re|\Lambda|$ and decreases over a distance of $a/(Re|\Lambda|)$. The surface vorticity has a sine dependence on θ. The agreement with the theoretical predictions for $\Lambda < 0$ is good; taking into account the influence of flow boundedness improves the agreement - notice the largest disagreement of 15% occurs with the highest magnitude of Λ.

6.1.2. *Sphere*

The boundary layer structure of the vorticity field for a sphere is shown in figure 12 for $Re = 1$. A sucking flow increases the rate at which vorticity decays from the sphere and also increase the magnitude on the surface of the cylinder; blowing generates the opposite trend. A comparison is shown in figure 12(b) for $\Lambda = 0, 1$ and 3 (taken from Cliffe & Lever (1985)); the agreement is good. Although the vorticity distribution is approximately a sine curve, there is a small asymmetry.

The trend for the boundary layer on a sphere follows that of the cylinder, for $Re = 100$. For a blowing flow, figure 13(a,b) shows the vorticity field along $\theta = \pi/2$ and on the surface of the sphere. The vorticity increases with distance from the sphere until it reaches a shear layer, represented as the maximum, and then decreasing rapidly outside.
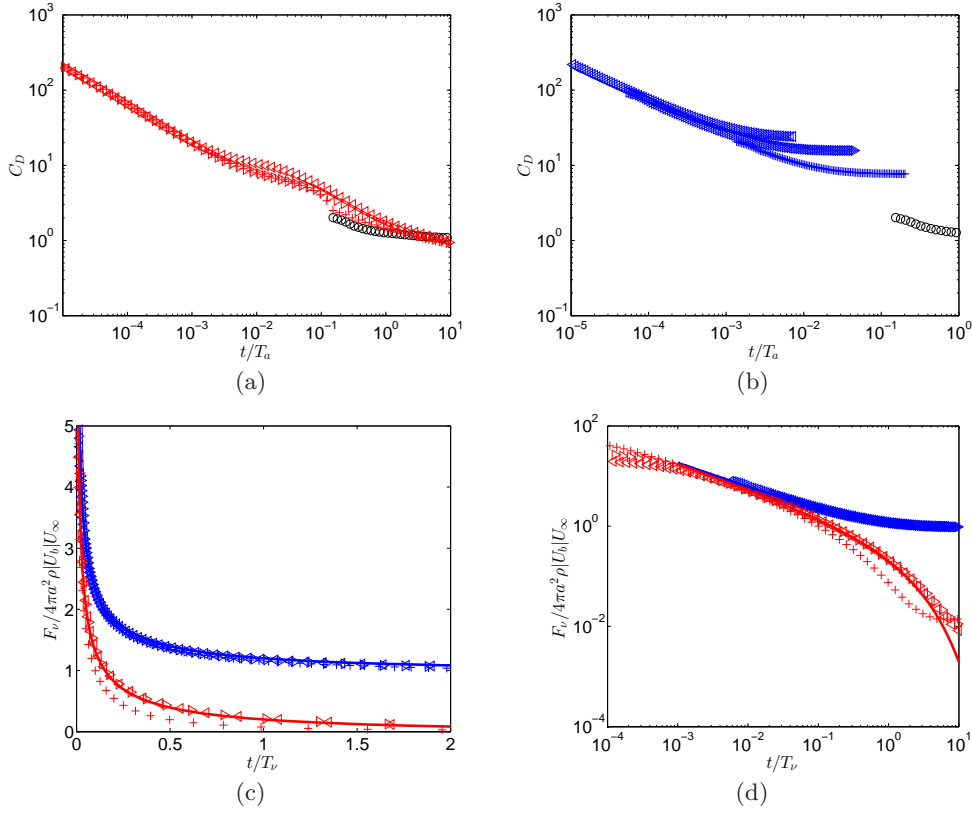
Figure 7: The characteristics of the drag force on a sphere at $Re = 100$ and $\Lambda = -3, -2, -1, 0, 1, 2$ and 3. In (a,b) the drag coefficient is show as a function of t, normalised by the advective timescale, for $\Lambda > 0$ and < 0 respectively. This The viscous component of the drag force is plotted in (c,d); to highlight the different decay rates (for long and short time), the viscous force is plotted on a linear scale in (c) and logarithmic scale in (d).

The position of the shear layer approximately scales as $\Lambda^{1/2}a$ for an axisymmetric flow. For a sucking flow, we see excellent agreement between the numerical calculations and (2.54). Since the influence of flow boundedness is greatly reduced for axisymmetric flows, the agreement for the distribution of vorticity on the surface is excellent, particularly at higher values of $|\Lambda|$.

6.2. *Vorticity flux*

The convective flux of vorticity from the surface of the cylinder is shown in figure 14. For $\Lambda < 0.5$, the convective flux of vorticity scales as $\Lambda^2 Re$ as confirmed in figure 14(a). Including a correction due to the boundedness of the domain (Appendix C), improves the agreement between the predictions and calculations. For blowing flows, we observe a weak dependence of the flux of vorticity on Λ. This is consistent with the scaling $\omega_s \sim U_\infty^2/U_b a$ observed in figure 4(d).
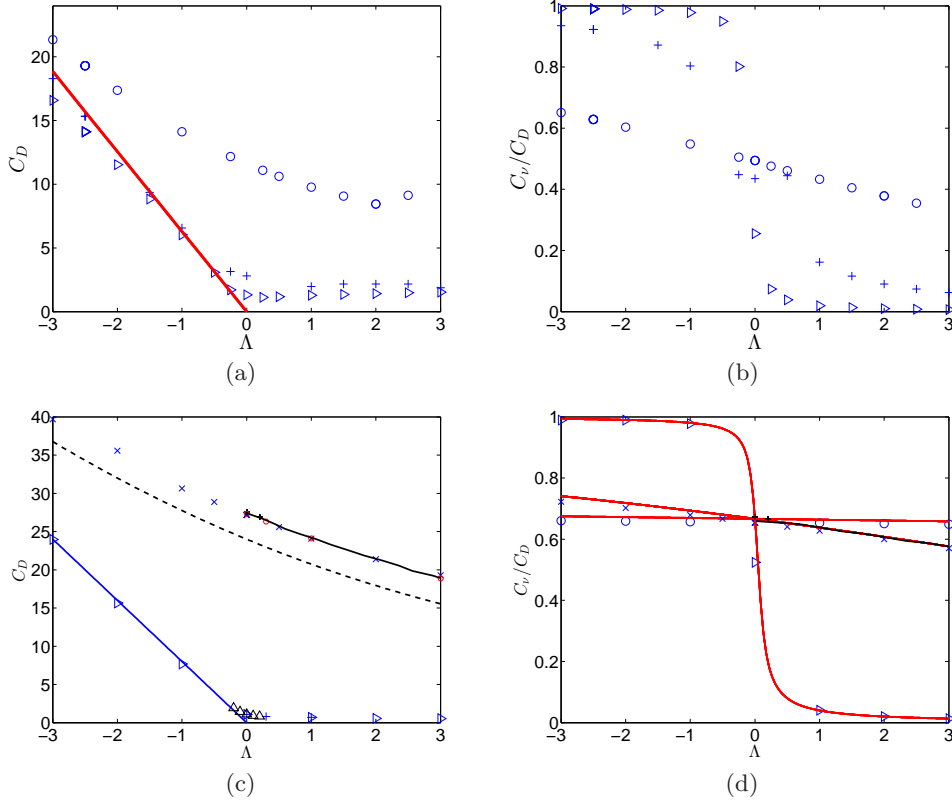
Figure 8: The influence of Λ on the drag coefficient for a cylinder and sphere are shown in (a,c) for $Re = 1, 10, 100$. The relative split between the viscous and total drag coefficient, as a function of Λ is shown in (b,d) indicating that the force is predominately viscous dominated for sucking flows ($\Lambda < 0$) and pressure dominated for blowing flows ($\Lambda > 0$). ○ corresponds to calculations in this paper. The red line is the asymptotic expression (2.59). The curves in (c,d) correspond to the analytical result from Dukowicz (1981).

6.3. *Pressure field*

6.3.1. *Cylinder*

The steady pressure distribution on the surface of the cylinder is shown in figure 15. For $\Lambda < 0$, the boundary is thin and the pressure is constant across the boundary layer, the surface pressure conforms to the irrotational prediction, as shown in figure 15(a). For $\Lambda = 0$ (figure 15(d)), the pressure distribution conforms closely to the potential flow prediction at the front of the cylinder, with an approximately constant pressure distribution in the wake. The pressure distribution has a weak dependent on Λ for $\Lambda > 0$ (see figure 15(b)), and this is consistent with the scalings §2.5.

6.3.2. *Sphere*

The steady pressure distribution on the surface of the sphere is shown in figure 15. For $\Lambda < 0$, the boundary is thin and the pressure is constant across the boundary layer, the surface pressure conforms to the irrotational prediction, as shown in figure 15(a). For $\Lambda = 0$ (figure 15(d)), the pressure distribution conforms closely to the potential flow prediction at the front of the cylinder, with an approximately constant pressure

(a)   (b)
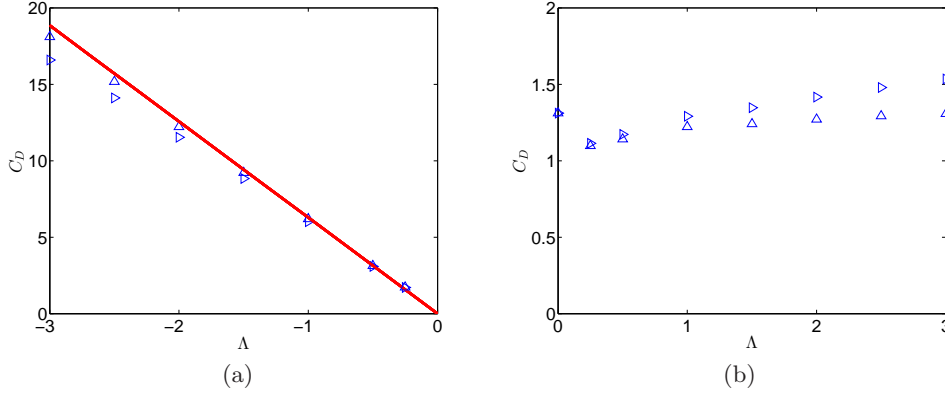
Figure 9: The steady drag coefficient for a cylinder at $Re = 100$ is plotted as a function of Λ as $\triangleright$. The drag coefficient is corrected for flow boundedness and plotted in (a,b) as $\triangle$ for $\Lambda < 0$ and $\Lambda > 0$, where the corrected drag coefficient is $C_{D_\infty} = C_D(1 + \Delta U/U_\infty)$ and $C_{D_\infty} = C_D(1 + \Delta U/U_\infty)^2$
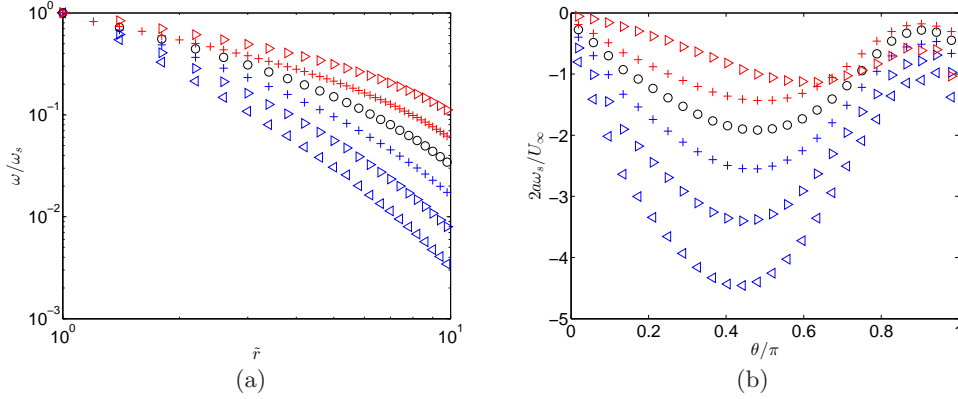

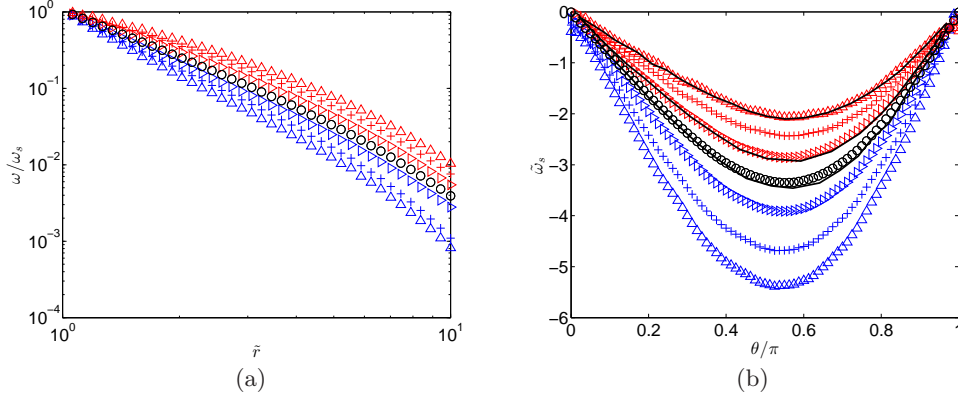(a)   (b)

Figure 10: Vorticity distribution in the boundary layer of a cylinder at $Re = 1$, for $\Lambda = -3, -2, -1, 0, 1, 2$ and 3. In (a), the vorticity through the boundary layer along the line of $\theta = \pi/2$, normalise by its value at $\tilde{r} = 1$. In (b), the vorticity distribution over the surface of the cylinder.

distribution in the wake. The pressure distribution has a weak dependent on $\Lambda > 0$ (see figure 15(b)), and this is consistent with the scaling (2.85).

7. Flow field

7.1. *Cylinder*

Figure shows the vorticity distribution and streamlines in the vicinity of a cylinder. For $\Lambda > 0$, the vortex sheets that are formed by the blowing flow separating the positive and negative vorticity which is then advected downstream. The vorticity decreases due to local cross-stream diffusion. Further downstream the vortex shear layers become unstable and form a von Kármán vortex sheet. For $\Lambda < 0$, the boundary layer is extremely thin and is
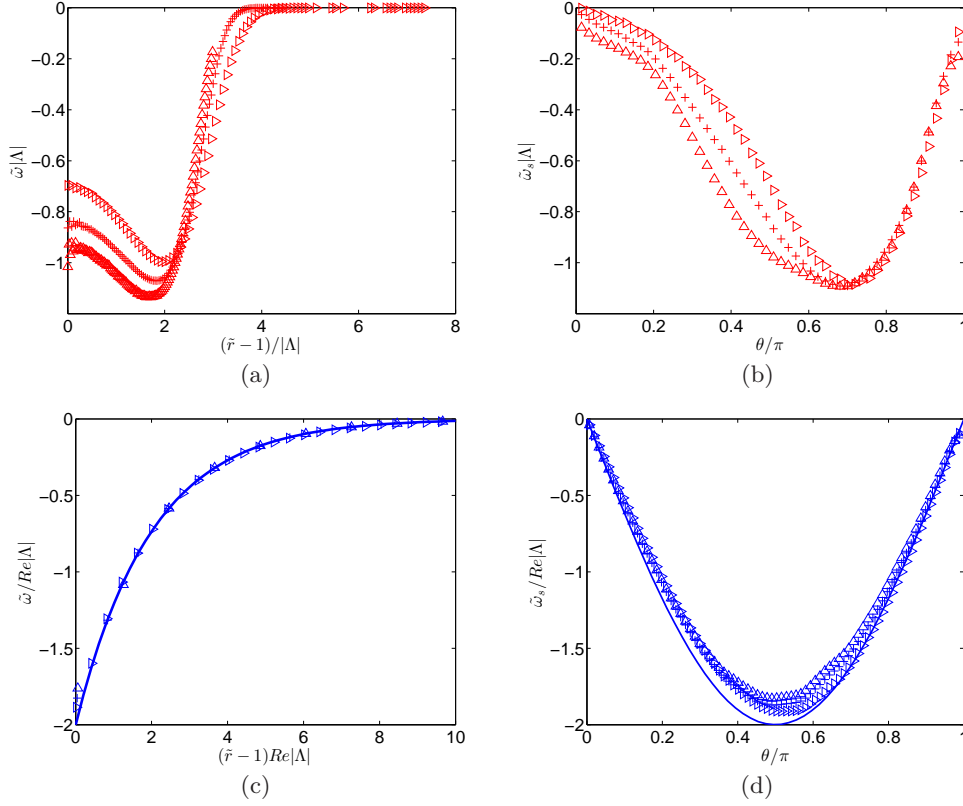
Figure 11: Vorticity distribution in the boundary layer of a cylinder at $Re = 100$, in (a,b) and (c,d) for $\Lambda = 1, 2, 3$ and $-3, -2, -1$ respectively. In (a,c) the vorticity through the boundary layer, along the line $\theta = \pi/2$, is plotted; while in (b,d) the vorticity on the surface of the cylinder is plotted. The blue curve in (c,d) corresponds to (2.53).

localised around the cylinder surface. Outside the boundary layer, the flow is irrotational; this is also maintained downstream for sufficiently strong enough sucking flow.

7.2. *Sphere*

Figure shows the vorticity distribution downstream of a sphere. The calculations are axisymmetric and reflected along the central axis For $\Lambda > 0$, the vortex sheets that are formed by the blowing flow separating the positive and negative vorticity which is then advected downstream. The flow calculations are axisymmetric and this stabilises the presence of the wake bubble that is initially seen in behind a cylinder.

8. Conclusions

In this paper we have examined the influence of a uniform through-surface flow on the flow past a rigid cylinder and sphere and the forces they experience. The new part of the analysis is a more detailed study over a wider parameter regime, particularly the influence of a strong through flow, and a detailed analysis of the steady and unsteady forces which the bodies experience.

To summarise:

(a)   (b)

Figure 12: Vorticity distribution in the boundary layer of a sphere at $Re = 1$, for $\Lambda = -3, -2, -1, 0, 1, 2$ and 3. In (a), the vorticity through the boundary layer along the line of $\theta = \pi/2$, normalise by its value at $\tilde{r} = 1$. In (b), the vorticity distribution over the surface of the sphere. The full curves correspond to the results of Cliffe & Lever (1985) for $\Lambda = 0, 1, 3$.

a) for sucking flows, the boundary layer is established in a viscous timescale of T_ν. The boundary layer initially grows as $\delta_\nu \sim (\nu t)^{1/2}$ and tends to a thickness $\delta_\nu \sim \nu/|U_b|$. The drag coefficient for a cylinder and sphere decay as $1/t^{1/2}$, initially dominated by viscous forces and ultimately tends to a constant where the drag force is given by ( ) and proportional to the sucking velocity, ie $F_D \to -\rho A_b U_\infty U_b$, since the wake volume flux is negligible. The pressure on the surface of the pressure corresponds to the irrotational flow prediction and has a negligible contribution to the total force on the body. The calculated vorticity distribution over the surface of the cylinder and sphere and through the boundary layer agree with the theoretical predictions at high Re. The vorticity on the surface ω_s shows a sin dependence on angular position and decays exponentially through the boundary layer and scales as $\omega_s \sim |U_b|U_\infty/a\nu$.

b) for blowing flows, the boundary layer initially has a thickness at/U_b, then growing at a rate $a(t/T_b)^{1/D}$ until it settles down to a constant thickness which scales as $\Lambda^{1/(D-1)}a$. The viscous component shows a $1/t^{1/2}$ decay for both cylinders and spheres; the pressure component has a $1/t^{1/(D-1)}$ dependence before tending to a constant. The viscous force is negligible at high Re. In contrast to the sucking flow, the drag force shows a weaker dependence on $\Lambda(> 0)$. The vorticity on the surface of the body scales as $U_\infty^2/|U_b|a$. The flux of vorticity through the surface has a weak dependence on U_b. After the vorticity is swept from the surface, it forms a pair of opposite signed local vortex sheets separated by a distance $\Lambda^{1/(D-1)}a$, which can be infered by from a potential flow analysis. They combine through an instability which occurs at a distance $\Lambda^{1/(D-1)}a$ downstream. The strength of the vorticity decays through viscous diffusion, before combining and forming a vortex street (in the case of a cylinder). The three-dimensional instability does not occur in the axisymmetric calculations, but as we see from Bagadi, one of the few three-dimensional flow calculations for a blowing sphere, a similar sort of instability will ultimately occur.

To understand these flow processes, a cascade of models were developed using a momentum flux argument, analysis of the viscous stresses and pressure distribution, and dissipation argument to examine the total drag for sucking and these have elucidated the key mechanisms and are in agreement with the numerical results. For the blowing case, scaling analysis and conformal mapping have been applied to the cylinder problem,
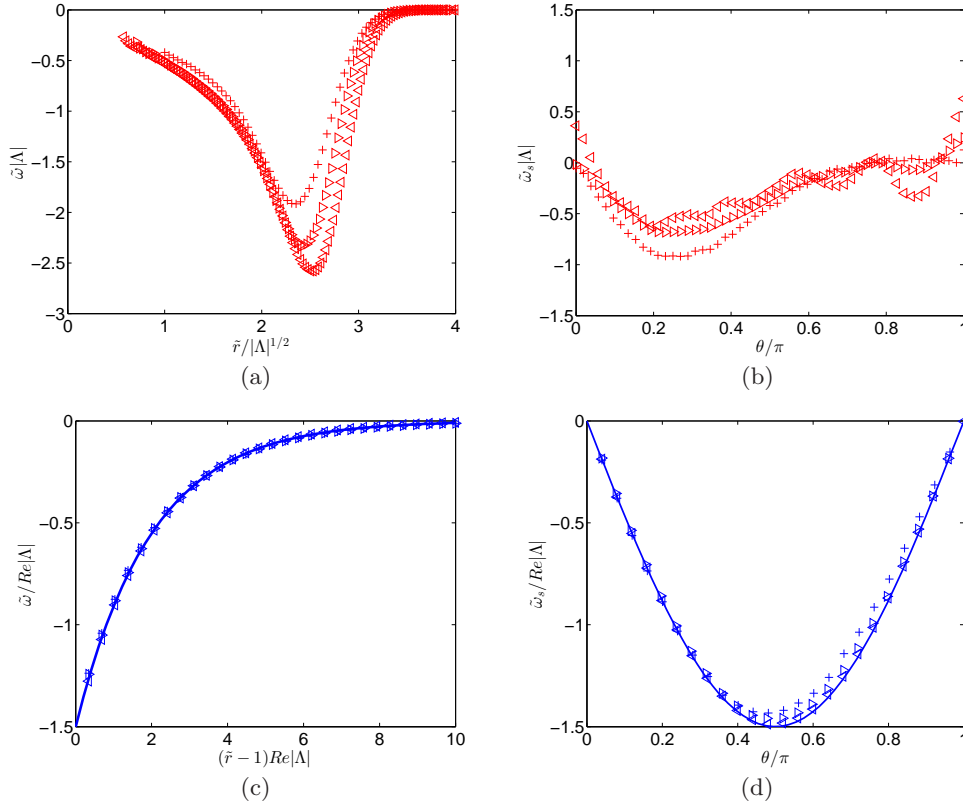
Figure 13: Vorticity distribution in the boundary layer of a sphere at $Re = 100$, in (a,b) and (c,d) for $\Lambda = 1, 2, 3$ and $-3, -2, -1$ respectively. In (a,c) the vorticity through the boundary layer, along the line $\theta = \pi/2$, is plotted; while in (b,d) the vorticity on the surface of the sphere is plotted. The blue curve in (c,d) corresponds to (2.53).

while scaling analysis has been applied to the blowing case. The initial boundary layer structure for blowing captures the viscous process, while an inviscid analysis captures some elements of the initial boundary layer blown away for high Re. There have been a number of significant hurdles in broadening the parameter range studies (see figure 1), in particular for high through-flow velocities. The extremely thin boundary layer generate on a rigid surface for high sucking velocities and the dependence of the drag force (for $|\Lambda| > 1$) on the size of the computational domain represented a significant computational challenge, which partially explains the absence of published research for $\Lambda < -0.5$, despite the available models from the 1950's.

The study in this paper is of a uniform through-surface flow applied to bluff bodies, complementing the work in the 1950s on the drag properties of porous cylinders and also the evaporation of spherical droplets. But more generally, a through-surface flow is applied to control the heat transfer properties of turbine blades and the lift/drag properties of lifting surfaces. In these cases, the characteristics Reynolds numbers are number higher and the through-surface flow is only applied over portions to their surface. Future studies should focus on influence of a through-surface flow, partially applied to streamline bodies, on their lift / drag characteristics.
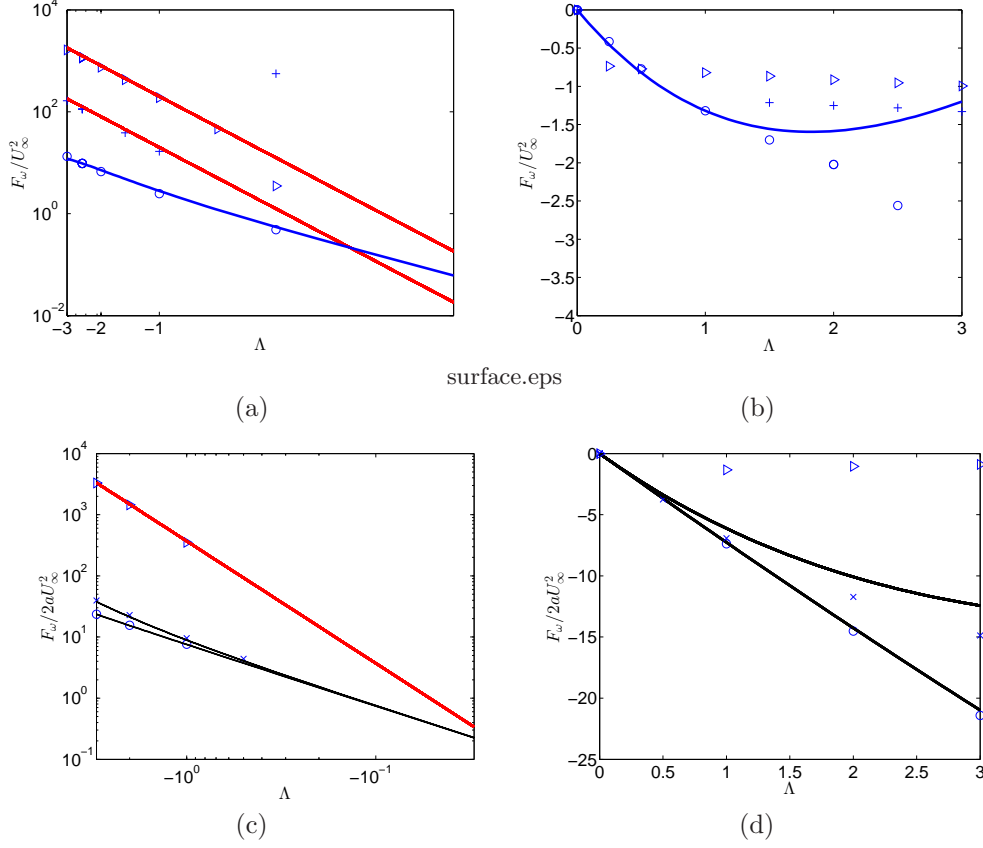
Figure 14: Vorticity flux

Appendix A: Drag force acting on a rigid body with sucking

To show that (2.56) is equivalent to (2.58), we need only to demonstrate that

$$I \equiv \int_{S_B} \frac{\partial \phi}{\partial s} n_y \mathrm{d}S = U_\infty P, \qquad (A1)$$

where P is the perimeter or surface area of the body, $Q_s = -U_b P$. In two-dimensions, (A1) can be rewritten as,

$$I = \int_{S_B} \left(\frac{\partial \phi}{\partial x} \frac{\mathrm{d}x}{\mathrm{d}s} + \frac{\partial \phi}{\partial y} \frac{\mathrm{d}y}{\mathrm{d}s} \right) \frac{\mathrm{d}x}{\mathrm{d}s} \mathrm{d}s, \qquad (A2)$$

where s is the distance along the surface. The kinematic condition requires that the $u_n = \frac{\partial \phi}{\partial x} \frac{\mathrm{d}y}{\mathrm{d}s} - \frac{\partial \phi}{\partial y} \frac{\mathrm{d}x}{\mathrm{d}s} = 0$, so that

$$I = \int_{S_B} \frac{\partial \phi}{\partial x} \left[\left(\frac{\mathrm{d}x}{\mathrm{d}s} \right)^2 + \left(\frac{\mathrm{d}y}{\mathrm{d}s} \right)^2 \right] \mathrm{d}S = U_\infty P_\infty + \int_{S_B} (U_x - U_\infty) \mathrm{d}s. \qquad (A3)$$

For a two-dimensional body, symmetric about the x-axis, the second term is zero by symmetry and (A1) is recovered. A similar approach can be adopted for an axisymmetric body, whose shape is $R(x)$ in cylindrical coordinates. By definition, the surface integral
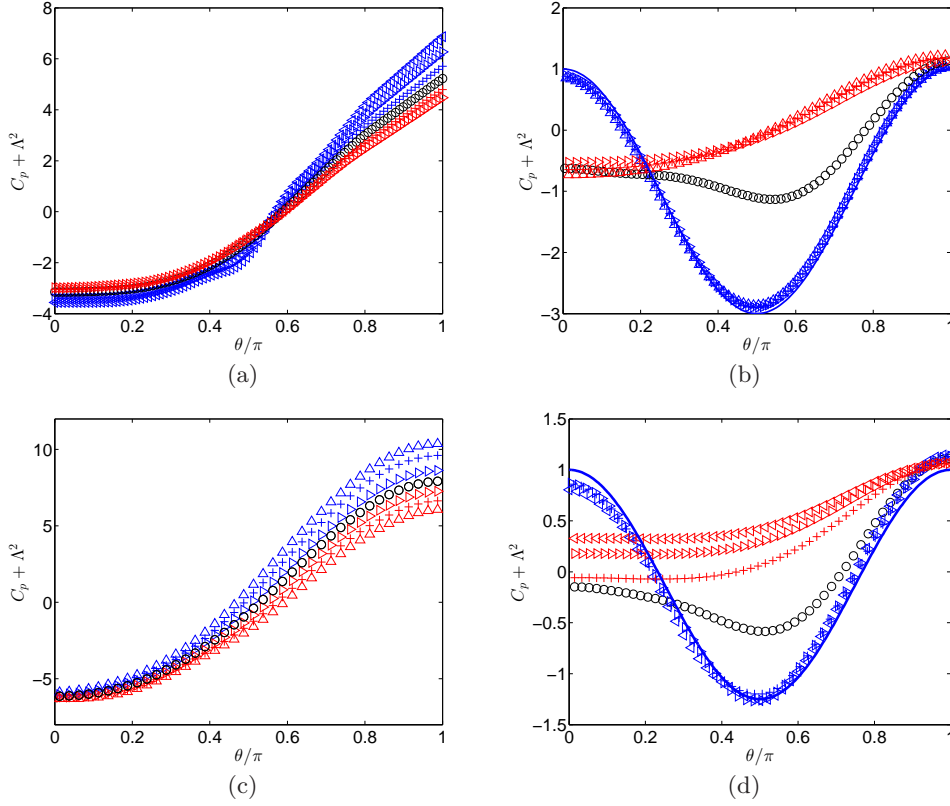
Figure 15: Pressure distribution on the surface of a (a,b) cylinder and (c,d) sphere. In (a,c), $Re = 1$, while for (b,d), $Re = 100$. The full curves in (b,d) correspond to (2.54) and () respectively.

I can be expressed as

$$I \equiv \int_{S_B} \left(\frac{\partial \phi}{\partial x} \frac{\mathrm{d}x}{\mathrm{d}s} + \frac{\partial \phi}{\partial R} \frac{\mathrm{d}R}{\mathrm{d}s} \right) \mathrm{d}S = \int_{S_B} 2\pi R \mathrm{d}s U_\infty + \int_{S_B} (U_x - U_\infty) \, 2\pi R \mathrm{d}s.$$

By symmetry, the second term is zero and the identity ($A1$) holds.

Appendix B: Axisymmetric formulation

The axisymmetric formulation is similar to the planar case (see Nicolle & Eames (2011), Appendix A), but the integration is taken over a volume obtained by sweeping the elements around the axis of symmetry. The Navier-Stokes equation for an axisymmetric flow (u_r, u_z) is

$$\rho \left(\frac{\partial u_r}{\partial t} + u_r \frac{\partial u_r}{\partial r} + u_z \frac{\partial u_r}{\partial z} \right) = -\frac{\partial p}{\partial r} + \mu \left(\frac{1}{r} \frac{\partial}{\partial r} \left(r \frac{\partial u_r}{\partial r} \right) + \frac{\partial^2 u_r}{\partial z^2} \right) - \frac{u_r}{r^2},$$

$$\rho \left(\frac{\partial u_z}{\partial t} + u_r \frac{\partial u_z}{\partial r} + u_z \frac{\partial u_z}{\partial z} \right) = -\frac{\partial p}{\partial z} + \mu \left(\frac{1}{r} \frac{\partial}{\partial r} \left(r \frac{\partial u_z}{\partial r} \right) + \frac{\partial^2 u_z}{\partial z^2} \right),$$

C.A. Klettner, I. Eames, S. Semsarzadeh, & A. Nicolle

(a)

(b)

(c)

(d)

(e)

(f)

(g)
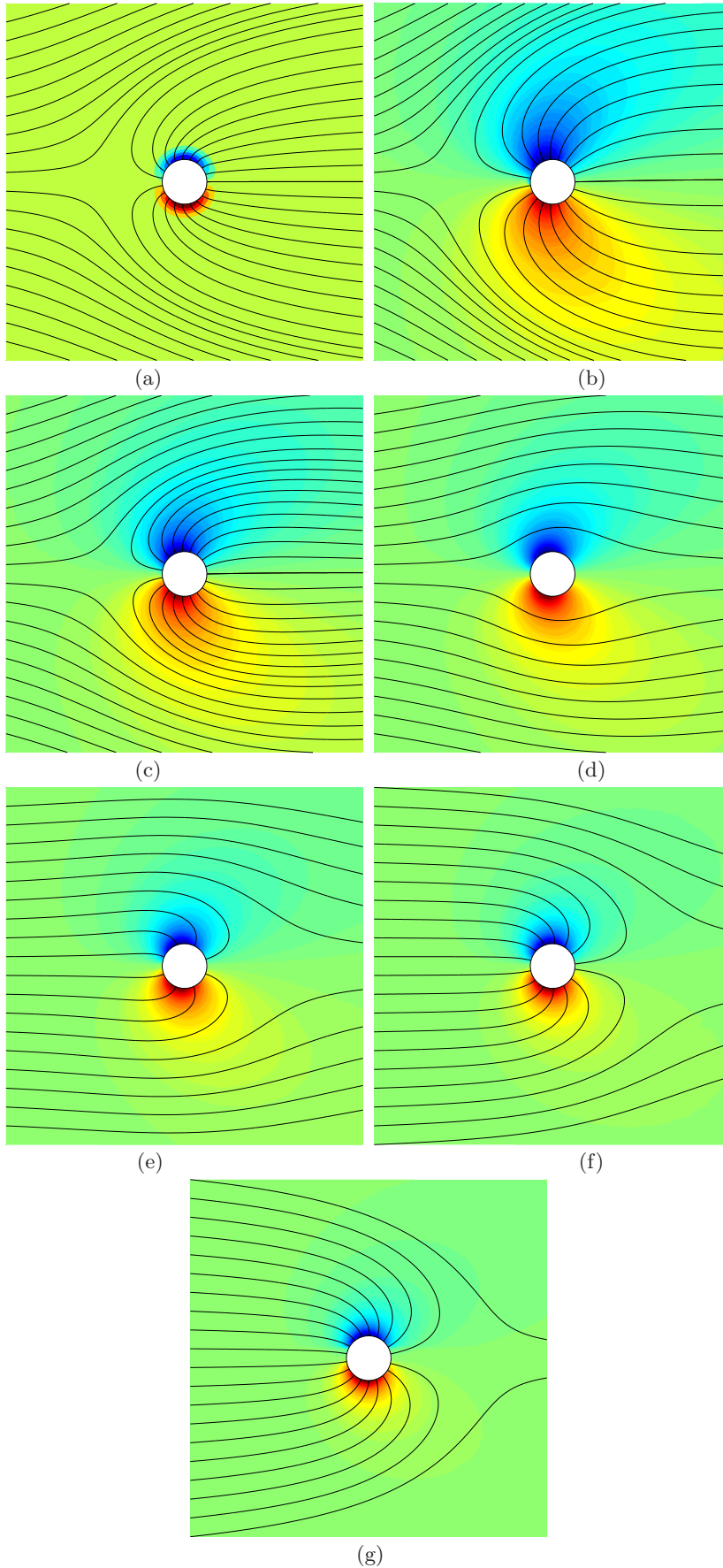
Figure 16: Vorticity field around a cylinder for $Re = 1$ and (*a*) $\Lambda = -3$, (*b*) -2, (*c*) -1 and (*d*) 1. The vorticity is normalised so its value extends over the range -1 to 1.
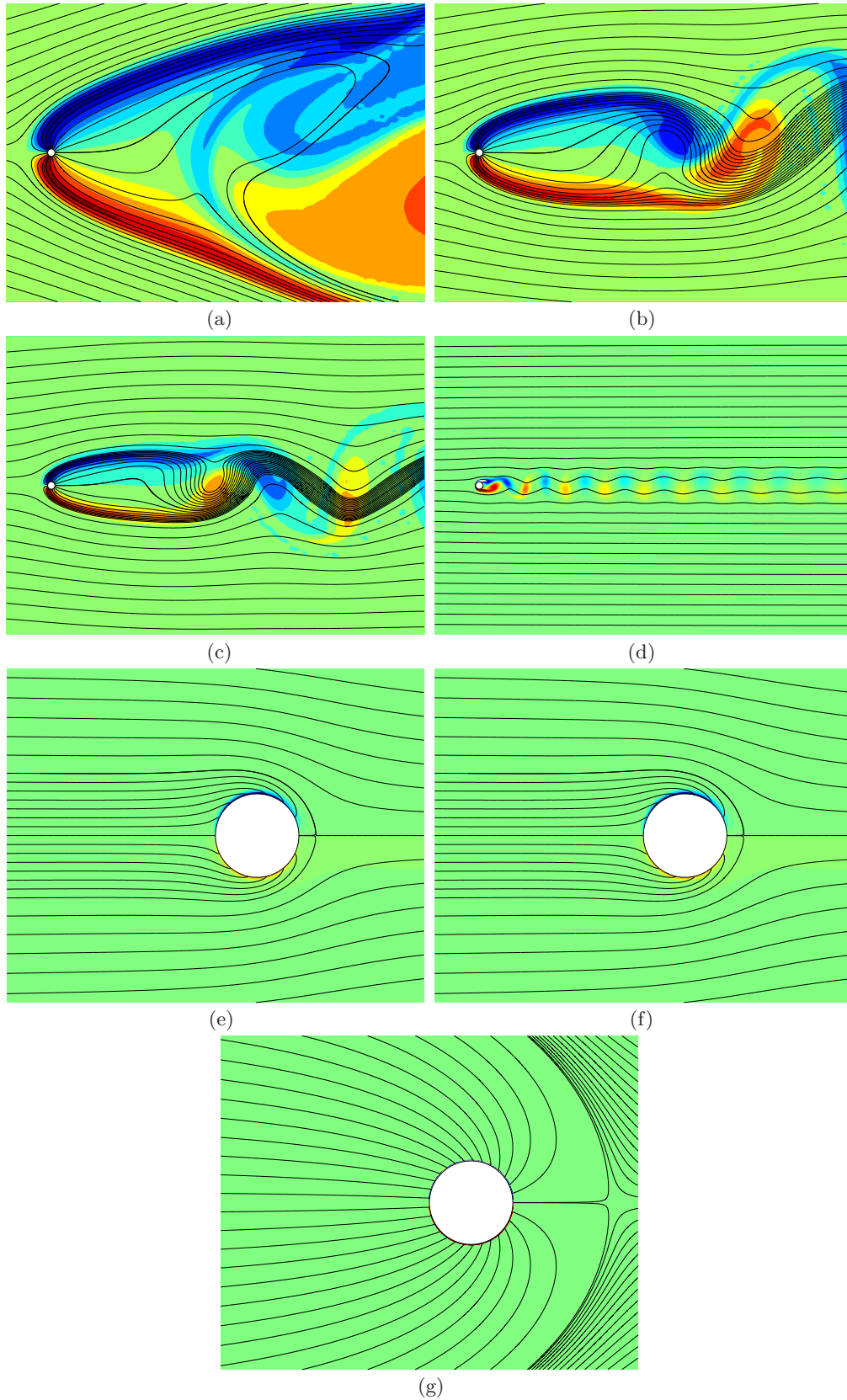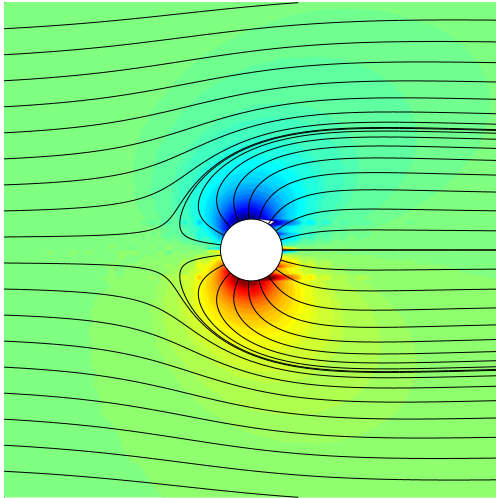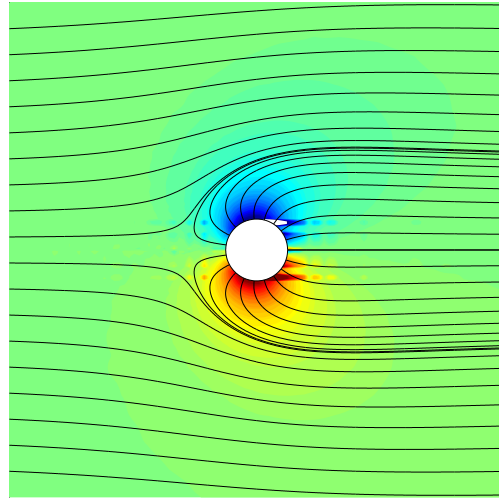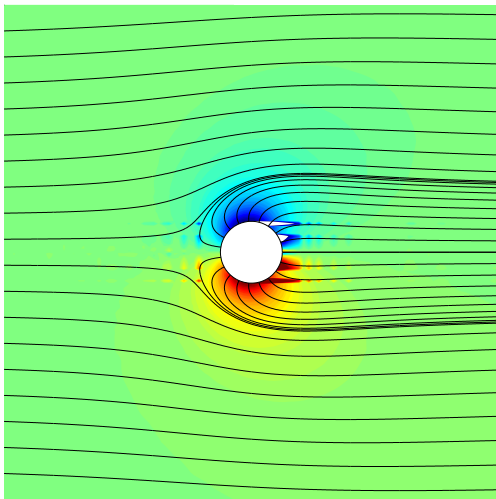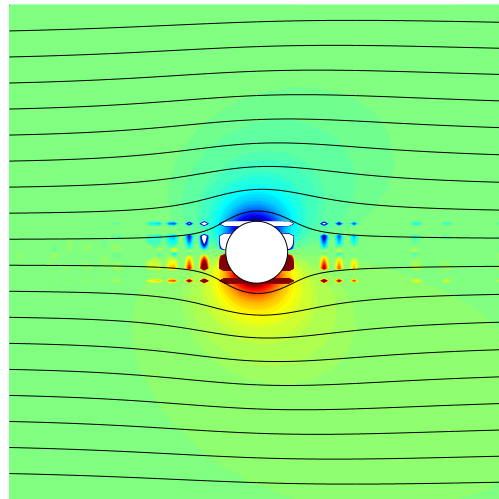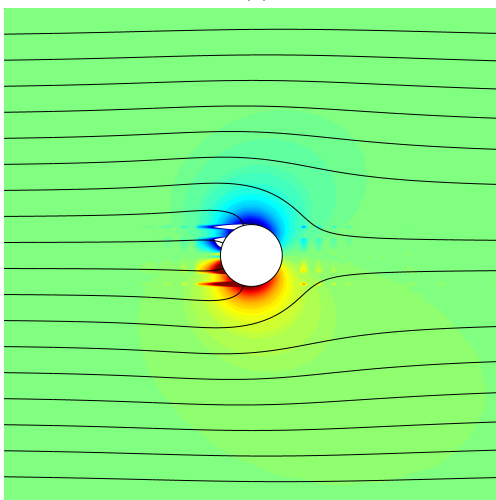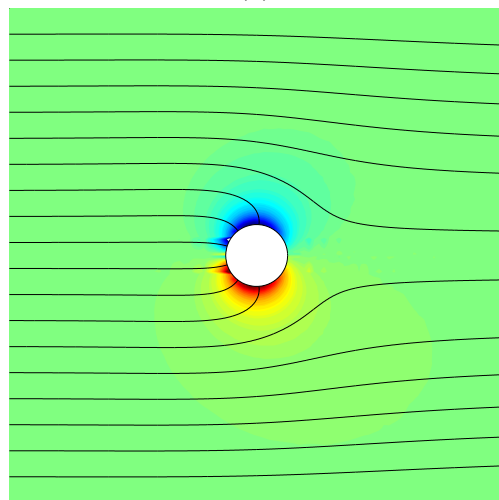
Figure 17: Vorticity field around a cylinder for $Re = 100$ and (a) $\Lambda = -3$, (b) -2, (c) -1 and (d) 1. The vorticity is normalised so its value extends over the range -1 to 1.
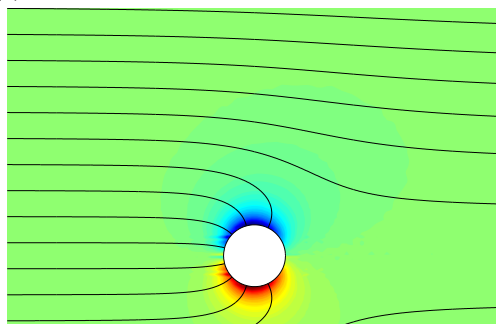
(a)   (b)
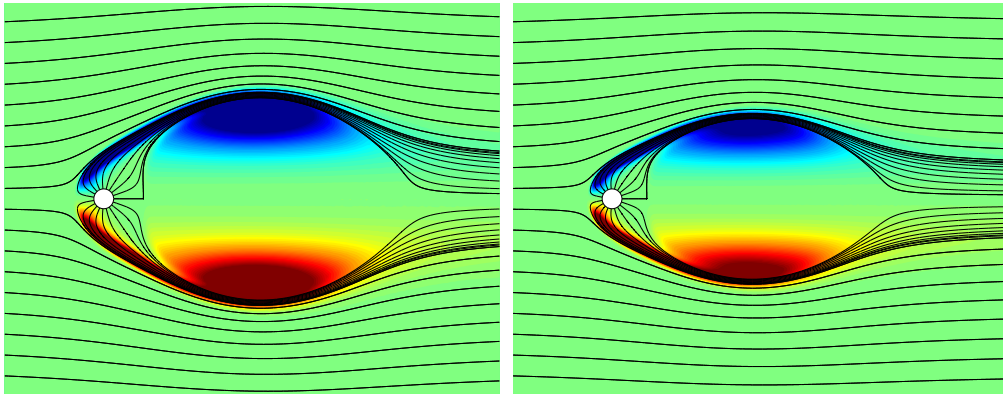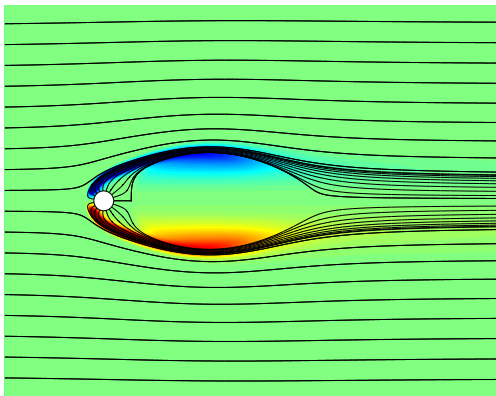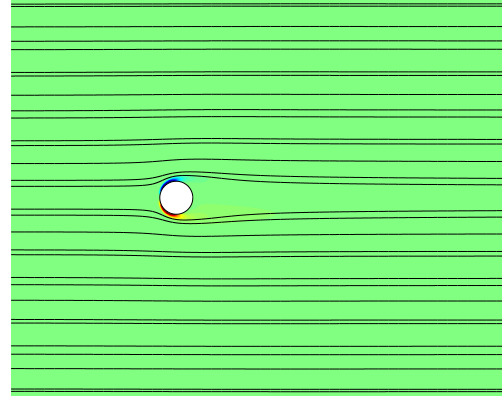
(c)   (d)

(e)   (f)
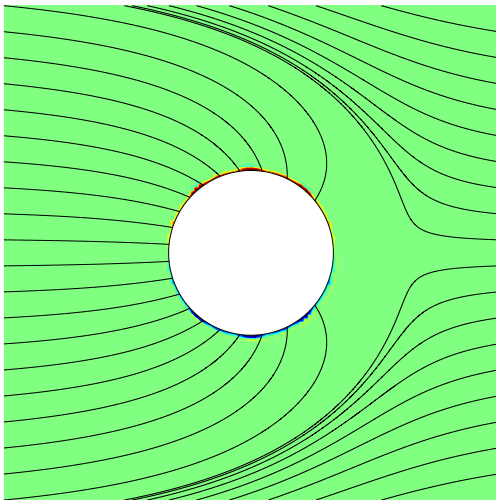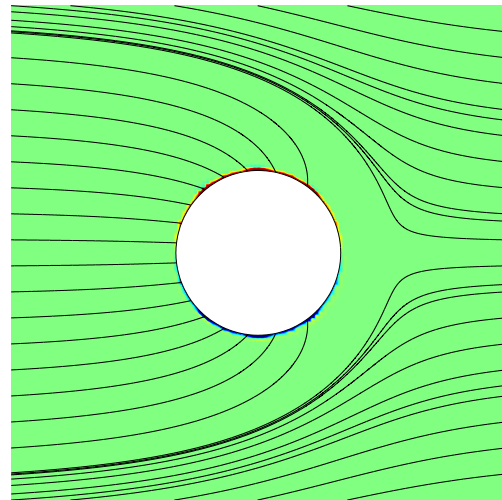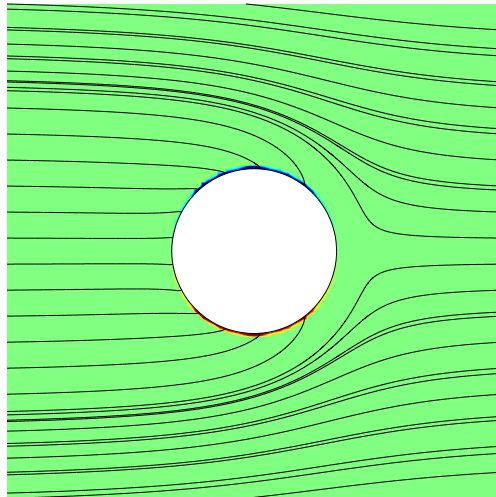
(a)

(b)

(c)

(d)

(e)

(f)

(g)

where r and z are the radial and axial positions respectively. The mass conservation equation is

$$\frac{1}{r}\frac{\partial}{\partial r}(ru_r) + \frac{\partial u_z}{\partial z} = 0.$$

The Characteristic Based Split (CBS) scheme is a well-known method of numerically solving the Navier-Stokes equation. A set of linear basis functions, $[\boldsymbol{N}] = [N_i, N_j, N_k]$, are introduced which depend on z and r. Within each triangular element, the velocity and pressure components are $u_z = [\boldsymbol{N}]\{\boldsymbol{u}_z\}$ and $u_r = [\boldsymbol{N}]\{\boldsymbol{u}_r\}$ such that $\partial[\boldsymbol{N}]/\partial r = \boldsymbol{b}/2A$ and $\partial[\boldsymbol{N}]/\partial z = \boldsymbol{c}/2A$, where A is the area of the local element. In the CBS scheme, three numerical steps are applied between t^n and t^{n+1}:

Step 1: Momentum solve

$$[\boldsymbol{M}]\frac{\tilde{\boldsymbol{u}}_r - \boldsymbol{u}_r^{(n)}}{\Delta t} = -[\boldsymbol{K}_C]\{\boldsymbol{u}_r\}^{(n)} - \nu[\boldsymbol{K}]\{\boldsymbol{u}_r\}^{(n)} - \frac{\nu}{r^2}[\boldsymbol{M}]\{\boldsymbol{u}_r\}^{(n)} - [\boldsymbol{K}_S]\{\boldsymbol{u}_r\}^{(n)} + \nu[\boldsymbol{F}]\{\boldsymbol{u}_r\}^{(n)}, \tag{C1}$$

and

$$[\boldsymbol{M}]\frac{\tilde{\boldsymbol{u}}_z - \boldsymbol{u}_z^{(n)}}{\Delta t} = -[\boldsymbol{K}_C]\{\boldsymbol{u}_z\}^{(n)} - \nu[\boldsymbol{K}]\{\boldsymbol{u}_z\}^{(n)} - [\boldsymbol{K}_S]\{\boldsymbol{u}_z\}^{(n)} + \nu[\boldsymbol{F}]\{\boldsymbol{u}_z\}^{(n)}. \tag{C2}$$

Step 2: Pressure solve

$$[\boldsymbol{K}]\{\boldsymbol{p}\}^{(n+1)} = -\frac{\rho}{\Delta t}\left([\boldsymbol{G}_r]\{\tilde{\boldsymbol{u}}_r\} + \frac{1}{r}[\boldsymbol{M}]\{\tilde{\boldsymbol{u}}_r\} + [\boldsymbol{G}_z]\{\tilde{\boldsymbol{u}}_z\}\right) + [\boldsymbol{F}]\{\boldsymbol{p}\}.$$

Step 3: Velocity correction

$$[\boldsymbol{M}]\{\boldsymbol{u}_r\}^{(n+1)} = [\boldsymbol{M}]\{\tilde{\boldsymbol{u}}_r\} - \frac{\Delta t}{\rho}[\boldsymbol{G}_r]\{\boldsymbol{p}\}^{(n+1)},$$

and

$$[\boldsymbol{M}]\{\boldsymbol{u}_z\}^{(n+1)} = [\boldsymbol{M}]\{\tilde{\boldsymbol{u}}_z\} - \frac{\Delta t}{\rho}[\boldsymbol{G}_z]\{\boldsymbol{p}\}^{(n+1)}.$$

The local formulations on each element requires the evaluation of the following matrices and vectors:

$$[\boldsymbol{M}] = \frac{2\pi r A}{12}\begin{bmatrix}2 & 1 & 1\\1 & 2 & 1\\1 & 1 & 2\end{bmatrix}, \quad [\boldsymbol{K}_C] = \frac{[\boldsymbol{M}]}{2A}\left(\{\boldsymbol{u}_r\}\{\boldsymbol{b}\} + \{\boldsymbol{u}_z\}\{\boldsymbol{c}\}\right),$$

$$[\boldsymbol{K}_S] = \frac{[\boldsymbol{M}]\{\boldsymbol{u}_r\}\Delta t}{8A^2}\left[\{\boldsymbol{u}_r\}^T\boldsymbol{b}^T\boldsymbol{b} + \{\boldsymbol{u}_z\}^T\boldsymbol{b}^T\boldsymbol{c}\right] + \frac{[\boldsymbol{M}]\{\boldsymbol{u}_z\}\Delta t}{8A^2}\left[\{\boldsymbol{u}_r\}^T\boldsymbol{c}^T\boldsymbol{b} + \{\boldsymbol{u}_z\}^T\boldsymbol{c}^T\boldsymbol{c}\right]$$

$$[\boldsymbol{K}] = \frac{2\pi r}{4A}\left[\boldsymbol{b}^T\boldsymbol{b} + \boldsymbol{c}^T\boldsymbol{c}\right], [\boldsymbol{G}_r] = 2\pi r\begin{bmatrix}1\\1\\1\end{bmatrix}\boldsymbol{b}, [\boldsymbol{G}_z] = 2\pi r\begin{bmatrix}1\\1\\1\end{bmatrix}\boldsymbol{c}, [\boldsymbol{G}_{r2}] = 2\pi\begin{bmatrix}1\\1\\1\end{bmatrix}\boldsymbol{b}.$$

The forcing term is

$$[\boldsymbol{F}] = \frac{1}{2A}\int_{\Gamma_e}\left(\boldsymbol{N}^T n_1 d\Gamma \boldsymbol{b} + \boldsymbol{N}^T n_2 d\Gamma \boldsymbol{c}\right).$$

The boundary conditions are Dirichlet which are stenciled onto the global matrix.

REFERENCES

ABRAMOWITZ, M. & STEGUN, I.A. eds. 1972 Handbook of Mathematical Functions with Formulas, Graphs, and Mathematical Tables. New York: Dover Publications, ISBN 978-0-486-61272-0

BAGHCHI, P. 2007 Flow past a sphere with surface blowing and suction. *Journal of Fluids Engineering.* **129** 1547–1558

BAINES, W.D. & JAMES, D.F. 1994. Evaporation of a droplet on a surface 33: 411–416.

BASHKATOV, M.V. & SHABANOV, S.I. 1975 Flow around and heat and mass transfer of a sphere with blowing at medium Reynolds numbers. *J. Applied Mech. Tech. Phy.* **16**, 604–611.

BATCHELOR, G.K. 1967 An introduction to fluid dynamics. Cambridge University Press.

BAZANT, M.Z. & MOFFATT, H.K. 2005 Exact solutions of the Navier-Stokes equations having steady vortex structures. *J. Fluid Mech.* **541**, 55–64.

BETZ, A. 1925 A method for the direct determination of profile drag. *Z. Flugtechn. Motorluftschi*ahrt.* **16**, 42 (in German).

BOGARD, D.G. & THOLE, K.A. 2006 Gas turbine film cooling. *J. Propulsion and Power.* **22**, 249–270.

CASTRO, I.P. 1971 Wake characteristics of two-dimensional perforated plates normal to an air-stream. *J. Fluid Mech.* **46**, 599–609.

CROWE, C.T. 1976 Conservation equations for vapour-droplet flows including boundary-droplet effects. *Phd Thesis.* Lawrence Livermore Laboratory. University of California.

DUKOWICZ, J.K. 1981 An exact solution for the drag of a sphere in low Reynolds number flow with strong uniform suction or blowing. *Phys. Fluids*, **25**, 1117–1118.

EAMES, I. 2010 Momentum conservation and condensing vapor bubbles. *J. Heat Transfer*, **132**, 091501.

ECKERT, E.R.G. & LIVINGOOD, J.N.B. 1953 Method for calculation of laminar heat transfer in air flow around cylinders of arbitrary cross section including large temperature differences and transpiration cooling. NACA Report 1118, 223–251.

FRANSSON, J.H.M., KONIECZNYB, P. & ALFREDSSON, P.H. 2004 Flow around a porous cylinder subject to continuous suction or blowing. *J. Fluids and Structures*, **19**, 1031–1048.

GEUZAINE, C. & REMACLE, J.-F. 2009 Gmsh: a three-dimensional finite element mesh generator with built-in pre- and post-processing facilities. *Int. J. Numerical Methods in Eng.* **79**, 1309–1331.

GOWARD, G.W. 1998 Progress in coatings for gas turbine airfoils. *Surface & Coatings Technology.* **108–109**, 73–79.

HAMIELEC, A.E., HOFFMAN, T.W. & ROSS, L.L. 1967 Numerical solution of the Navier-Stokes equation for flow past spheres: Part I. Viscous flow around spheres with and without radial mass efflux. *AIChE J.* **13**, 212–219.

HUNT, J.C.R. & EAMES, I. 2002 The disappearance of laminar and turbulent wakes in complex flows. *J. Fluid Mech.* **457**, 111–132.

HURLEY, D.G. & THWAITES, M.A. 1951 An experimental investigation of the boundary layer on a porous circular cylinder. British Aeronautical Research Council, Reports and Memoranda No. 2829.

IACOVIDES, H. & LAUNDER, B.E. 1995 Computational fluid dynamics applied to internal gas-turbine blade cooling: a review. *Int. J. Heat & Mass Flow.* **16**, 454–470.

HOWE, M.S. 1995 On the force and moment produced by a body in an incompressible fluid, with application to rigid bodies and bubbles at high and low Reynolds numbers. *Q. J. Mech. Appl. Maths.* **48**, 401–426.

LAMB, H. 1932 Hydrodynamics. Dover Press.

LANDAU, L.D. & LIFSHITZ, E.M. 1987 Fluid Mechanics. Vol. 6 (2nd ed.). *Butterworth Heinemann.*

LAUGA, E., BRENNER, M.P. & STONE, H.A. 2007 Microfluidics: The no-slip boundary condition. in Handbook of Experimental Fluid Dynamics (Chapter 19) C. Tropea, A. Yarin, J. F. Foss (Eds.), Springer, 2007. ISBN: 978-3-540-25141-5.

CLIFFE, K.A. & LEVER, D.A. 1985 Isothermal flow past a blowing sphere. *Int. J. Numerical Methods in Fluids.* **5**, 709–725.

LEVICH, V.G. 1949 The motion of bubbles at high Reynolds numbers. Zh. Eksp. Teor. Fiz.

19, 18; see also *Physiochemical Hydrodynamics*, English translation by Scripta Technica, Prentice-Hall, Englewood Cliffs, NJ, 1962, p. 436.

LING, G.P. & FANG, J.W. 2000 Numerical study on the flow around a circular cylinder with surface suction or blowing using vorticity-velocity method. *Applied Mathematics & Mechanics*, **23**, 1089–1096.

MATHELIN, L., BATAILLE, F. & LALLEMAND, A. 2002 The effect of uniform blowing on flow past a circular cylinder. *Trans. A.S.M.E.* **124**, 452–464.

MOORE, D.W. 1963 The boundary layer on a spherical gas bubble. *J. Fluid Mech.* **16**, 161–176.

NICOLLE, A. & EAMES, I. 2011 Numerical study of flow through and around a circular array of cylinders. *J. Fluid Mech.* **679**, 1–31.

NISHINO, T. & SHARIFF, K. 2012 Effect of Jet Nozzle Lip Momentum Loss on Circulation Control Airfoil Performance. *A.I.A.A.*, **50**, 551–558.

NITSCHE, M. & KRASNY, R. 1994 A numerical study of vortex ring formation at the edge of a circular tube. *J. Fluid Mech.* **216**, 139–161.

PANKHURST, R.C., THWAITES, B. 1953 Experiments on the flow past a porous cylinder fitted with a Thwaites Flap. *Aero. Res. Council Reports and Memoranda.* R.& M. 2787 (A.R.C. Technical Report). 29pp.

REYNOLDS, O. 1886 On the theory of lubrication and its application to Mr Beauchamp Towers experiments, including an experimental determination of the viscosity of olive oil. *Phil. Trans. R. Soc. Lond.* **177**, 157–234.

SAFFMAN, P.G. 1992 Vortex Dynamics. *Cambridge University Press.*

TOMBOULIDES, A. G., AND S. A. ORSZAG 2000. Numerical investigation of transitional and weak turbulent flow past a sphere. *J. Fluid Mech.* **416**, 45–73.

ROTTMAN, J.W. & SIMPSON, J.E. 1983 Gravity currents produced by instantaneous releases of a heavy fluid in a rectangular channel. *J. Fluid Mech.* **135**, 95–110.

STONE, H.A. 1992 An interpretation of the translation of drops and bubbles at high Reynolds numbers in terms of the vorticity field. *Physics of Fluids*, **5**, 2567–2569.

ZIENKIEWICZ, O.C., TAYLOR, R.L. & NITHIARASU, P. 2005 The Finite Element Method for Fluid Dynamics. *Butterworth-Heinemann.*

ZHANG, H. 2004 Numerical research on a vaporising fuel droplet in a forced convection environment. *Int. J. Multiphase Flow.* **30**, 181–198.

ZHAO, F., HARRINGTON, D.C. & LAI, M.-C. 2002 Automotive gasoline direct-injection engines. *Society of Automotive Engineers.* ISBN 0-7680-0882-4